Azimuthal offsets in spiral arms of nearby galaxies

Miguel Querejeta¹, Sharon E. Meidt², Yixian Cao³, Dario Colombo⁴, Eric Emsellem^{5,6}, Santiago García-Burillo¹, Ralf S. Klessen^{7,8,9,10}, Eric W. Koch¹¹, Adam K. Leroy¹², Marina Ruiz-García^{1,13}, Eva Schinnerer¹⁴, Rowan Smith¹⁵, Sophia Stuber¹⁴, Mallory Thorp⁴, Thomas G. Williams¹⁶, Médéric Boquien¹⁷, Daniel A. Dale¹⁸, Chris Faesi¹⁹, Damian R. Gleis¹⁴, Kathryn Grasha²⁰, Annie Hughes²¹, María J. Jiménez-Donaire^{22,1}, Kathryn Kreckel²³, Daizhong Liu²⁴, Justus Neumann¹⁴, Hsi-An Pan²⁵, Francesca Pinna^{26,27}, Alessandro Razza²⁸, Toshiki Saito²⁹, Jiayi Sun³⁰, and Antonio Usero¹

(Affiliations can be found after the references)

Received / Accepted

ABSTRACT

Spiral arms play a central role in disc galaxies, but their dynamical nature remains a long-standing open question. Azimuthal offsets between molecular gas and star formation are expected if gas crosses spiral arms, as predicted by quasi-stationary density wave theory. In this work, we measure offsets between CO and H α peaks in radial bins for 24 galaxies from the PHANGS survey that display a well-delineated spiral structure. The offsets exhibit substantial scatter, implying that star formation is not exclusively initiated at a coherent spiral shock. We define offsets such that positive values mean H α peaks lie ahead of CO peaks in the direction of galactic rotation. With this convention, 14 galaxies show mean positive CO-H α offsets, typically of a few hundred parsecs. In four of these 14 galaxies (17% of the total), offsets become smaller with increasing radius, as expected for a single quasi-stationary spiral density wave. Ten galaxies (42%) show positive mean offsets but no clear correlation with radius, which is compatible with multiple overlapping modes. In the remaining ten galaxies (42%), we find no significantly positive offsets, which could point to transient dynamical spirals or material arms, where gas and stars co-rotate with the spiral perturbation. Across the full sample, we find mostly positive offsets between CO peaks and the gravitational potential minimum, confirming that gas often crosses the spiral perturbation. For the four galaxies with clear positive offsets and a radial trend, we derived pattern speeds in good agreement with the literature. Overall, our results suggest that even well-delineated spirals in the local Universe can arise from a variety of underlying dynamical mechanisms.

Key words. galaxies: spiral - galaxies: structure - galaxies: ISM - galaxies: star formation

1. Introduction

Despite the widespread presence of spiral arms in the local Universe (e.g. Nair & Abraham 2010; Willett et al. 2013; Buta et al. 2015), understanding their origin and nature remains an open subject of research in contemporary astrophysics. One of the most popular theories to explain the spiral pattern in disc galaxies is quasi-stationary spiral density wave theory (Lin & Shu 1964, 1966; Bertin et al. 1989; Bertin 2000), which posits that spiral arms are long-lived, self-sustaining modes of the disc that rigidly rotate at a constant pattern speed, Ω_P . In this model, spiral arms are local overdensities formed by different stars over time as gas and stars cross the spirals.

In another leading theory, spirals are temporary material patterns that rotate with the disc. This would be the case for spirals originating through swing amplification (Goldreich & Lynden-Bell 1965; Julian & Toomre 1966; Meidt & van der Wel 2024) or spirals that are tidal features produced during interactions and mergers (e.g. Toomre 1969, 1981; Donner & Thomasson 1994; Kawata et al. 2014). The former are thought to be consistent with the spirals in flocculent galaxies, whereas the latter are argued to be prominent in some grand-design spirals, such as M51 (especially in the outer regions; Meidt et al. 2009, Tress et al. 2020). In either case, in contrast to the Lin-Shu quasi-stationary modes, material spirals are temporary features of the disc, and they co-rotate with the disc material (Dobbs & Baba 2014; Sell-

wood & Masters 2022) such that the gas and stars do not cross the spiral.

The spirals formed in modern simulations of isolated disc galaxies exhibit properties resembling both types of theory: They are short-lived rigidly rotating 'groove' modes of the disc shaped by both swing amplification (which amplifies small perturbations as they shear due to differential rotation) and changes to the disc properties brought about by earlier spiral features (Sellwood & Carlberg 2014; see also Binney 2020; Sridhar 2019; Meidt & van der Wel 2024; Hamilton 2024). These spirals are often composed of multiple independent modes, each excited around its own co-rotation. Observational measurements of multiple independent pattern speeds (e.g. Meidt et al. 2008, 2009; Font et al. 2011, 2014, 2024; Colombo et al. 2014; Marchuk 2024) tend to support this picture, especially when the co-rotation resonance of one spiral overlaps with a resonance of another spiral (Sellwood & Carlberg 2014). Resonance overlaps such as these, which are also thought to allow for non-linear mode coupling (Sygnet et al. 1988), produce radially extended spiral arms that allow for energy and angular momentum transfer extending widely across the disc (Masset & Tagger 1997).

The spirals produced in these different pictures yield different responses to the gas and the young and old stellar discs, which can offer a way to discriminate between them. In the picture of quasi-stationary density waves, the shock predicted in the gas as it overtakes the spiral pattern leads to a systematic offset between the accumulation of gas at the shock front

and star formation peaks and thus also between young and older stars (Roberts 1969). This offset will decrease in amplitude moving outwards along the spiral and switch direction, passing from inside to outside co-rotation. For multiple 'groove' modes that extend only out to co-rotation, no switch in offset location will be produced. For material arms, no systematic offset is expected (Grand et al. 2012a,b; Kawata et al. 2014; Baba et al. 2015).

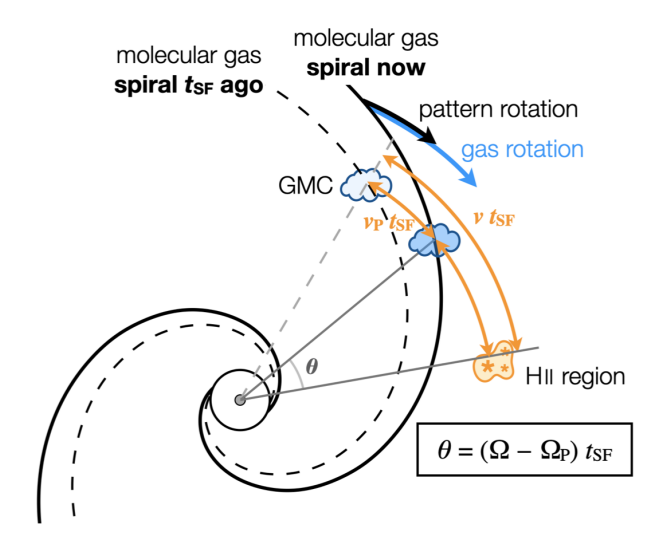
Numerous studies have attempted to identify angular offsets associated with spiral arms. Different approaches include measuring changes in pitch angle for several bands or colour maps (Grosbøl & Dottori 2009; Abdeen et al. 2020; Martínez-García et al. 2023; Marchuk et al. 2024b), identifying stellar populations or clusters of different ages (Choi et al. 2015; Chandar et al. 2017; Shabani et al. 2018; Peterken et al. 2019), pinpointing offsets involving HII regions (Egusa et al. 2009, 2017; Cedrés et al. 2013), deriving w cross-correlations for different tracers (Tamburro et al. 2008; Foyle et al. 2011; Schinnerer et al. 2013), and even conducting comparisons with numerical simulations (Dobbs & Bonnell 2007; Wang et al. 2015).

Based on the analysis of offsets or pitch angles, some studies have found strong evidence supporting quasi-stationary spiral density wave theory for certain galaxies (e.g. Egusa et al. 2009; Peterken et al. 2019; Miller et al. 2019; Abdeen et al. 2020; Martínez-García et al. 2023; Marchuk et al. 2024b). However, such offsets have not been found in other galaxies (e.g. Egusa et al. 2009; Foyle et al. 2011; Ferreras et al. 2012; Martínez-García & González-Lópezlira 2013; Choi et al. 2015; Chen et al. 2024; Marchuk et al. 2024a). Thus, the picture that emerges so far is that quasi-stationary density wave theory may apply to some spiral galaxies but not to others. The choice of tracers and methodology is critical, as Louie et al. (2013) have shown that apparent discrepancies in the nature of gas-star formation offsets in M51 (Tamburro et al. 2008; Egusa et al. 2009; Foyle et al. 2011) are due to the choice of tracer, specifically because HI enhancements in M51 do not trace compressed gas as much as a product of H₂ photodissociation close to star-forming regions. The conclusion of Louie et al. (2013) was that CO and H α are the optimal tracers when it comes to establishing offsets between gas and star formation in spiral arms. Another important caveat is resolution, as small offsets will be washed out if observations do not attain sufficient physical resolution. In this sense, Egusa et al. (2009) detected offsets in some galaxies but not in others and hypothesised that the limited resolution (~500 pc) and/or sensitivity of their CO data could explain the lack of measured offsets in some cases. In other words, they have suggested that spiral density wave theory might apply across their sample, but, possibly, the signature only becomes apparent for the galaxies with sufficient resolution and sensitivity. This motivates the interest of revisiting this problem with high-resolution and highsensitivity CO and H α data for a sample of nearby galaxies.

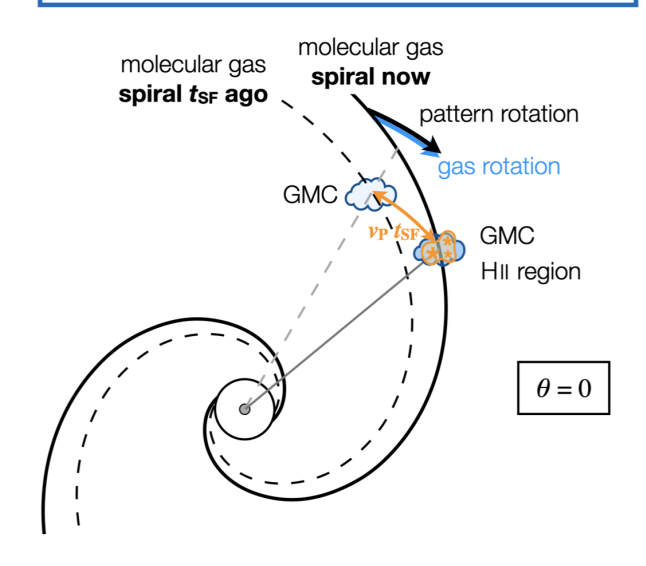
The main goal of this paper is to quantify CO-H α offsets in the PHANGS¹ sample of nearby galaxies. PHANGS provides the largest and highest resolution sample of nearby spiral galaxies with CO data to carry out this experiment (Leroy et al. 2021b), with an approximately five times higher physical resolution than Egusa et al. (2009). The structure of this paper is the following. In Sect. 2 we present the methodology and outline the main expectations for different scenarios that explain spiral structure. In Sect. 3 we describe our tracers of molecular gas and star formation. The main results of the paper are presented

in Sect. 4 and discussed in Sect. 5. We finish with a summary in Sect. 6.

quasi-stationary spiral density wave



material arms or dynamical spirals



Top panel: Quasi-stationary spiral density wave theory predicts azimuthal offsets in spiral arms. The thick solid black line shows the current position of the molecular gas spiral, while the dashed line displays its position, t_{SF} , earlier. If a shock coherently triggers the collapse of molecular gas along the spiral and if it takes t_{SF} for the resulting HII regions to be visible, the peaks of star formation will be displaced 'downstream' inside co-rotation. Measuring offsets at different galactocentric radii, one can calculate the (constant) pattern speed of the spiral and star formation timescale $t_{\rm SF}$ (Egusa et al. 2009). If multiple overlapping spiral modes are present in the disc, the situation illustrated in the top panel will apply for a limited radial range, with different pattern speeds operating at different radial zones. Bottom panel: Situation expected for material arms or dynamical spirals, where the spiral rotates at the same angular speed as the underlying disc material and therefore no bulk offsets are expected. In real galaxies, the fact that star formation is not limited to a coherent spiral shock introduces significant scatter in the offset measurements in both cases.

¹ Physics at High Angular resolution in Nearby GalaxieS; http://www.phangs.org

2. Methodology and expectations

According to the seminal work by Roberts (1969), spiral arms should result in a shock that triggers star formation as gas clouds get compressed (see also Roberts et al. 1975; Gittins & Clarke 2004). In the idealised case where star formation is exclusively initiated at the spiral shock, under spiral density wave theory we would expect systematic offsets between gas and star formation (except at co-rotation), as material travels a certain distance from the collapse of gas until star formation tracers are visible (e.g. $H\alpha$).

The ideal picture of star formation exclusively triggered at spiral arms is ruled out by observations, because stars also form in interarm regions (Foyle et al. 2010; Querejeta et al. 2021, 2024; Williams et al. 2022b) and star formation in spirals is not only initiated by a coherent shock, but also elongated structures such as spurs and feathers play an important role (Schinnerer et al. 2017). Furthermore, turbulence and feedback effects also modify the state of molecular gas locally and affect its ability to collapse and form stars (e.g. Federrath 2015; Krumholz 2015; Colman et al. 2025). Yet, stellar spiral arms do concentrate gas and, indirectly, star formation (Vogel et al. 1988; Garcia-Burillo et al. 1993; Sun et al. 2020; Querejeta et al. 2021, 2024; Sun et al. 2024). This means that while the departures from the ideal picture will induce scatter on the measurements, we do expect positive average offsets between CO and H α if gas crosses spiral arms. This is because more gas is accumulated and, on average, more star formation is initiated in the spiral region.

According to this picture, following quasi-stationary density wave theory, in the inner parts of galaxies $H\alpha$ peaks should be statistically displaced with respect to CO peaks in the direction of rotation. If the spiral pattern (density wave) rotates as a rigid structure with a constant pattern speed, these offsets are expected to decrease with increasing radius, all the way out to co-rotation, where the relative ordering of the tracers should flip. Following Egusa et al. (2009), Fig. 1 illustrates how offsets at a certain galactocentric radius will depend on the disc rotation at that radius (angular speed of the disc material) compared to the rotation of the spiral perturbation (assumed to be a fixed pattern speed). Thus, measuring these offsets for different galactocentric radii allows for simultaneous fitting of the constant pattern speed, Ω_P , and the timescale of star formation, t_{SF} , which is also assumed to be constant. This is possible when plotting the offsets as a function of the angular frequency, $\Omega = v_{rot}/R$, which requires adopting a certain rotation curve, $v_{rot}(R)$. Numerical simulations relying on a fixed spiral potential confirm the expectation that the azimuthal offsets between tracers of gas and star formation should vary with galactocentric radius (Gittins & Clarke 2004; Baba et al. 2015), but the result for more flocculent models without a fixed and strong spiral potential is less clear (e.g. Foyle et al. 2011).

There are three basic scenarios for spiral structure that we would like to differentiate, and where the offset measurements can be informative, as illustrated by Fig. 2. The first one is the traditional Lin-Shu spiral density wave with a constant pattern speed across the disc; in this case, we expect to measure CO-H α offsets which vary radially (showing a linear trend with Ω) across the whole disc. The second scenario involves multiple overlapping rigid spirals, each with their own pattern speed, which result in a positive mean CO-H α offset (since disc material travels across the spiral but it is always inside co-rotation); however, we would not expect a consistent trend with radius (or Ω) across the disc. Finally, for material arms or dynamical spirals, offsets

should randomly scatter around zero since the material does not cross the spiral pattern, resulting in a zero mean offset.

Figure 2 also shows schematically how we measure azimuthal offsets in spiral arms. First, we define a set of bins in fixed intervals of galactocentric radius, which results in elliptical annuli in the plane of the sky (according to the disc inclination and position angle from the PHANGS sample table 1.6; Lang et al. 2020). The width of the radial bins is chosen to be the largest between the resolution of the CO and H α map; in most cases, this is limited by the beam of the CO map, which is typically $\sim 1''$ ($\sim 100 \,\mathrm{pc}$ at a distance of $\sim 20 \,\mathrm{Mpc}$). Within each radial bin, we define a number of boxes at azimuthal intervals matching the same physical resolution (the azimuthal angle is measured anti-clockwise in the plane of the galaxy). This means that closer to the centre, the number of boxes will be smaller, while at larger radii there will be many more boxes. Within each of these boxes, typically $\sim 100 \,\mathrm{pc} \times 100 \,\mathrm{pc}$, we calculate the average intensity on the CO and $H\alpha$ maps. Then, for each galactocentric elliptical annulus and within the footprint of each spiral mask, we identify the azimuth of the boxes with maximum mean intensity in CO and H α , respectively. This way, we derive the angular offset between CO and H α ($\phi_{\rm max}^{\rm CO} - \phi_{\rm max}^{\rm H}$) in the plane of the galaxy for each spiral arm as a function of galactocentric radius. To account for the direction of rotation of the galaxy, we multiply the offsets by $\eta = +1$ if the galaxy rotates clockwise, or $\eta = -1$ if the galaxy rotates anti-clockwise (assuming spiral arms are trailing). This is because we adopt the definition that positive offsets imply that H α peaks lie ahead of CO peaks in the direction of galactic rotation.

The expectation for offsets with respect to the potential minimum is less clear. According to Roberts (1969), the shock is located immediately before the potential minimum. Thus, for the inner parts of galaxies, the order of tracers should be CO peaks, then stellar mass peaks, and finally $H\alpha$ peaks, as we move from the concave to the convex part of the spiral (assuming the spirals are trailing). Yet, even in simulations with a rigidly rotating potential, the relative offset between gas peaks and the gravitational potential minimum is not as straightforward and depends on the sound speed of the gas (Dobbs 2007; Wada 2008). For completeness, we also report on offsets between the stellar mass peaks and CO peaks in Sect. 4.3.

3. Sample and data

We focus on the 23 spiral galaxies from PHANGS-ALMA (Leroy et al. 2021b) with a spiral mask in Querejeta et al. (2021); a CO map that extends beyond the end of the bar to cover, at least partially, the spiral arms (Sect. 3.1); and an H α image available from PHANGS (Sect. 3.2). We added M51 (NGC 5194), which was targeted by similar studies in the past (e.g. Egusa et al. 2017). As explained in Querejeta et al. (2021), we emphasise that this sample is biased towards grand-design spiral galaxies, as it mostly excludes flocculent discs, where the spiral structure is less clear. We carried out radially binned measurements of the angular offsets as explained in Sect. 2. We also employed stellar mass maps tracing the potential minimum (Sect. 3.3). As a sanity check, we considered JWST maps at $2 \mu m$ for some galaxies as an alternative tracer of stellar mass (Sect. 3.4). We measured the offsets within the footprint of the spiral masks presented in Sect. 3.5.

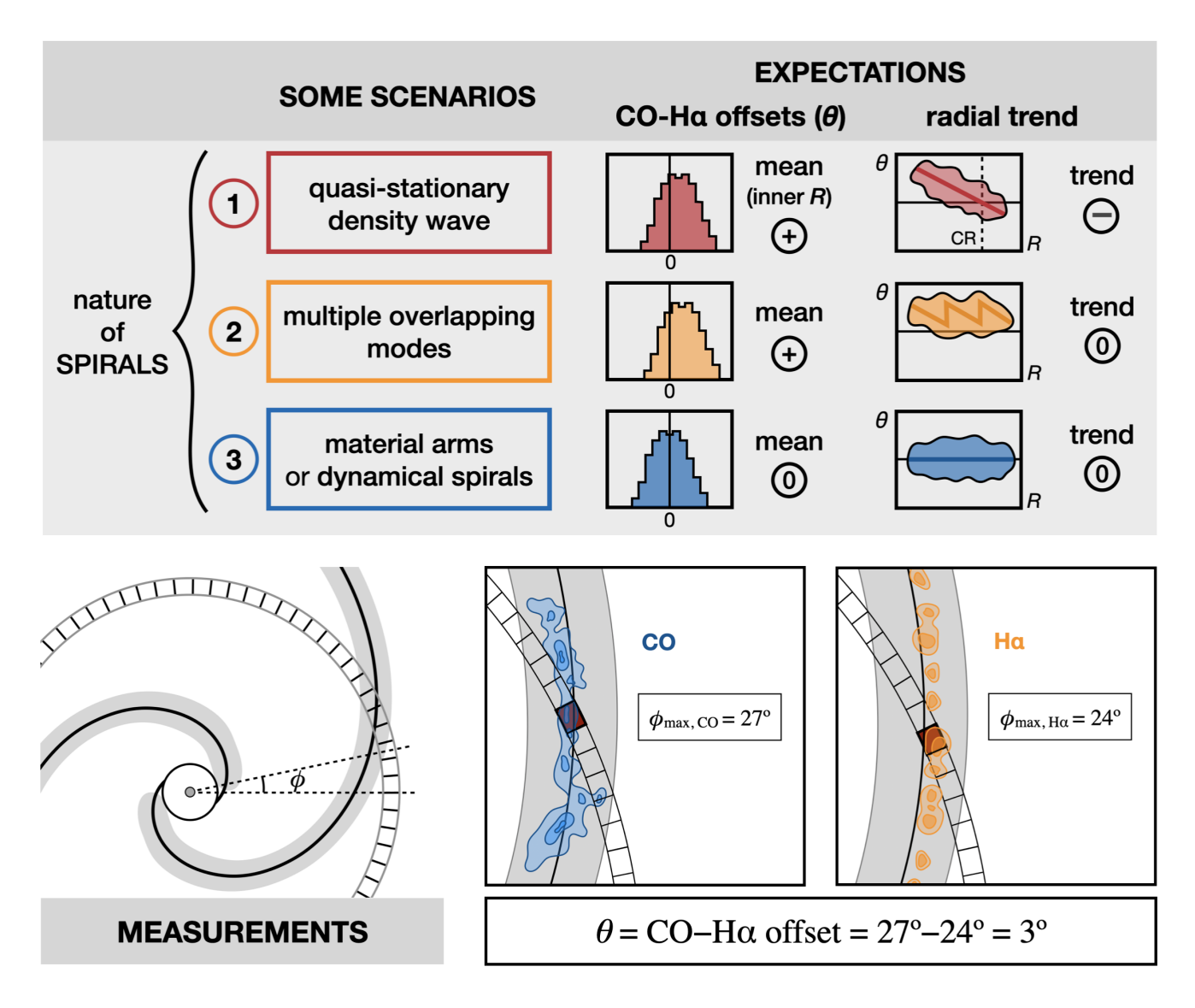


Fig. 2. Top: Illustration showing the expectations for a non-exhaustive list of three scenarios that explain spiral structure: a quasi-stationary density wave (constant pattern speed), multiple overlapping modes (i.e. different pattern speeds across the disc), and material arms (always made up of the same stars, all of which are by definition co-rotating) or dynamical spirals (transient features made up of rather short, unconnected segments). Middle panels: Expected histograms for the distribution of CO-Hα offsets (θ) as well as the expected mean offset. We define offsets such that positive values mean Hα peaks lie ahead of CO peaks in the direction of galactic rotation. For quasi-stationary density waves, we expect such offsets to be positive inside co-rotation and negative outside; however, since we sample mostly the inner parts of galaxies, the net offsets should typically be positive within our fields of view. The right panels indicate whether we should find a significant correlation between offsets and radius or not. Bottom: Illustration of how we measure azimuthal offsets in spiral arms in practice. For each radial bin (an elliptical annulus of width ~100 pc that accounts for the inclination and PA of the galaxy), we average the CO and Hα intensities in azimuthal bins. We then find the azimuth (φ) corresponding to the maximum of both tracers within the footprint of each spiral mask (φ_{max}). The angular difference between the bins of peak intensity yields the offset of interest, θ, at that radius. To account for galaxy rotation, if the galaxy rotates anti-clockwise, the offset θ is multiplied by $\eta = -1$.

3.1. CO as molecular gas tracer

We rely on ~1"-resolution (~100 pc) 12 CO(2–1) intensity maps from PHANGS–ALMA as a molecular gas tracer, which account for ~70% of all the CO emission in the galaxies (Leroy et al. 2021a). We consider the zeroth-order (integrated intensity) CO moment maps using the 'broad' masks presented in Leroy et al. (2021a) and publicly released in July 2022 (PHANGS–ALMA version 4.0). This provides high CO flux completeness, which makes it ideal for our purpose of determining offsets between peaks. We did not convert the CO integrated intensities to actual surface densities, as we are only interested in azimuthal offsets at fixed galactocentric radii and assume that $\alpha_{\rm CO}$ or R_{21} line ratio

variations at fixed radius and within the spiral region are negligible.

As a point of comparison with previous studies, we also considered M51 (NGC 5194) through the PAWS 12 CO(1–0) dataset (Schinnerer et al. 2013; Pety et al. 2013), using the publicly delivered zeroth-order moment map. PAWS provides a resolution of ~1" (~40 pc at the distance of M51).

3.2. $H\alpha$ as star formation tracer

Razza et al. (in prep.) obtained ground-based narrow-band $H\alpha$ images for a total of 65 galaxies from the PHANGS-ALMA par-

ent sample. These were observed with the Wide Field Imager (WFI) at the MPG 2.2-metre telescope in La Silla or with the DirectCCD camera at the du Pont 2.5-metre telescope in Las Campanas between 2016 and 2019 (these maps have been used e.g. in Pan et al. 2022). Both broad-band and narrow-band images were obtained, which allowed us to derive $H\alpha$ continuum-subtracted images. The resolution, limited by seeing, is typically ~1" (full width at half maximum, FWHM), ranging from 0.6" to 1.3".

Following Egusa et al. (2009), by default we consider offsets associated with H α flux peaks along spirals (which corresponds to a star-formation timescale of $\sim 5-10\,\mathrm{Myr}$; Kim et al. 2022). We did not apply any specific recipes to transform H α fluxes to actual star formation rates. While we are not concerned about the actual value of SFR, we are interested in locating the azimuthal peak of star formation around spiral arms, which could in principle be affected by extinction (we discuss this caveat in Sect. 5.4).

3.3. Spitzer IRAC 3.6 µm to trace stellar mass

In order to identify the minima of the gravitational potential, we used a set of stellar mass maps. For most galaxies, these are based on Spitzer 3.6 µm imaging obtained from the Spitzer Survey of Stellar Structure in Galaxies (S⁴G; Sheth et al. 2010), corrected for dust emission using an independent component analysis (ICA) technique (similar to principal component analysis, PCA). The method, introduced in Meidt et al. (2012), was applied to the entire S⁴G sample in Querejeta et al. (2015). It makes use of simultaneous $3.6 \,\mu\mathrm{m}$ and $4.5 \,\mu\mathrm{m}$ observations and exploits the fact that stellar and dust emission are expected to have very different [3.6]-[4.5] colours. Then, ICA identifies the global stellar and dust [3.6]-[4.5] colours that best describe the two underlying components. For the galaxies which are not in S^4G , we used the original IRAC 3.6 μ m maps (not corrected with ICA; see Querejeta et al. 2021 for details). We do not care about the actual conversion of NIR fluxes into stellar mass, since we only need to identify the local peaks, so we do not discuss the details of the mass-to-light (M/L) ratio. However, we note that a constant M/L on the ICA-corrected 3.6 µm maps is expected to yield a good representation of the stellar surface density according to Meidt et al. (2014).

3.4. Alternative tracers based on JWST imaging

In spiral arms, the stellar mass maps from Sect. 3.3 rely strongly on the ICA correction for dust emission, since the additional non-stellar emission is especially significant around star-forming regions. For this reason, as a sanity check, for a few galaxies we considered JWST maps at $2\,\mu{\rm m}$ as an alternative tracer of stellar mass. PHANGS-JWST observations are available for multiple bands, including NIRCam F200W, as part of a Cycle 1 JWST Treasury program (proposal 2107; PI: J. Lee). From our sample of spiral galaxies, those Cycle 1 observations cover NGC 0628, NGC 1300, NGC 1385, NGC 1512, NGC 1566, NGC 1672, NGC 3627, NGC 4303, NGC 4321, NGC 4535. (See Lee et al. (2023) and Williams et al. (2024) for additional information about the JWST observations and data reduction.)

3.5. Spiral masks

Throughout this paper, we use the spiral component of the environmental masks defined in Querejeta et al. (2021). These masks delimit morphological features visually identified on NIR

images which, in addition to spiral arms, include centres, bars, rings, lenses, and discs. For M51 (NGC 5194), we constructed a new spiral mask in full analogy to the masks released for PHANGS (Querejeta et al. 2021).

Specifically, spiral masks were constructed following three steps. Firstly, regions of bright $3.6\,\mu\mathrm{m}$ emission were identified along each spiral arm (using an unsharp-mask approach) and fitted with an analytic log-spiral function in the plane of the galaxy. Secondly, analytic log-spiral curves were assigned a width determined empirically based on CO emission. Finally, the resulting masks were visually inspected and the starting and ending point of some segments were extended in order to enforce continuity. For most galaxies, the NIR images and the analytic log-spiral fits come from S⁴G (Herrera-Endoqui et al. 2015), but we also relied on archival *Spitzer* $3.6\,\mu\mathrm{m}$ observations in some cases, where we also performed the log-spiral fitting, as explained in Querejeta et al. (2021).

The spiral masks from Querejeta et al. (2021) consist of smooth, dilated log-spiral segments, with a typical width of $\sim 1-2\,\mathrm{kpc}$ in order to accommodate most $3.6\,\mu\mathrm{m}$, CO, and $H\alpha$ emission along the arm. Locally, the distribution of molecular gas or star formation in the arms looks often thinner, but the presence of kinks and irregularities requires this width in order to warrant full coverage along the entire arm.

4. Results

We start by presenting our measurements of the CO– $\mathrm{H}\alpha$ offsets in Sect. 4.1. In Sect. 4.2 we examine any radial trends present in the offsets. Then, we consider the offsets with respect to the peak in stellar mass in Section 4.3. In Sect. 4.4 we take one step further and, for the galaxies with offsets that follow a consistent radial trend, we derive the star formation timescales and pattern speeds following Egusa et al. (2009).

4.1. Offsets between molecular gas and star formation

Figure 3 illustrates the CO-H α offsets in NGC 1566. As expected, if gas and stars cross the spiral perturbation, star formation is displaced towards the convex (leading) side of the western spiral compared to molecular gas. Yet, this displacement is far from constant. At some radial bins, HII regions are nearly cospatial with a CO peak (offset ~ 0), while most bins show typical offsets of a few hundred parsecs, up to a couple of kiloparsecs in the most extreme cases (e.g. at $R \sim 5$ kpc). By default we measure offsets between CO and H α peaks, but in Appendix B we consider instead mean intensity-weighted positions, which decreases the scatter, but conclusions are not affected. The right panel demonstrates how, despite the significant scatter, a bulk positive offset emerges for the inner radii, and the mean offset traced by the running means declines until a radius of $R \sim 9$ kpc, after which it becomes slightly negative. We opt for running means instead of running medians because we are interested in the bulk average offset with respect to zero, and not the typical offset at a given radius.

Most galaxies in our sample show positive mean CO-H α offsets in the plane of the galaxy, as illustrated in Fig. 4, which displays the statistical results for the whole sample. For each galaxy we calculate the average of all CO-H α offsets, considering all spiral arms simultaneously; the numerical results per galaxy are listed in Table 1. The typical mean offsets per galaxy are of several hundred parsecs (mean 230 pc, median 220 pc), ranging from -400 pc up to 740 pc. As a first simple test on

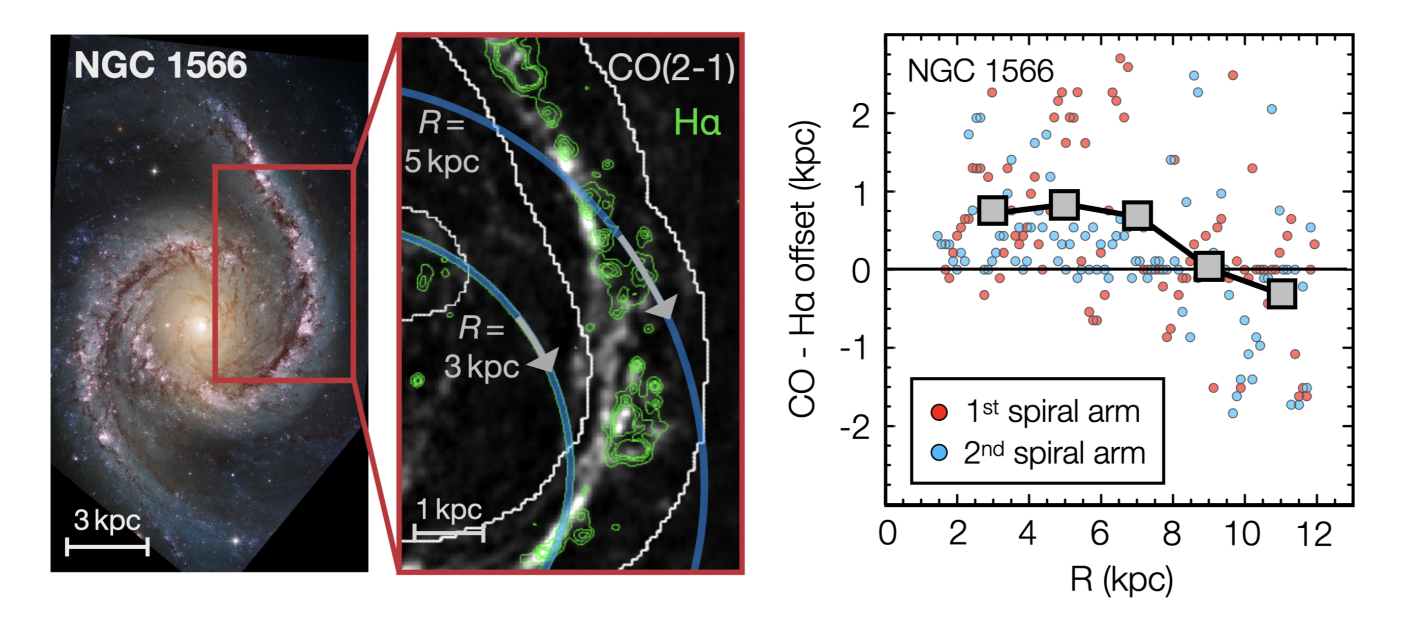


Fig. 3. Colour composite image of NGC 1566 based on six different HST WFC3/UVIS filters (Lee et al. 2023). The middle panel illustrates offsets in the western arm of NGC 1566 between molecular gas (CO, greyscale on background image) and star formation (H α , green contours). Blue shaded ellipses indicate two reference radial bins (R = 3 kpc and R = 5 kpc), the arrows indicate the sense of rotation, and white contours delimit the spiral mask. In the right panel, the radial distribution of all CO-H α offsets across the entire NGC 1566 are shown. The first spiral arm is the eastern arm; the second spiral arm is the western arm. The error bars are comparable to the size of the plotted circles. The gray squares show running means at radial intervals of 2 kpc (combining both arms).

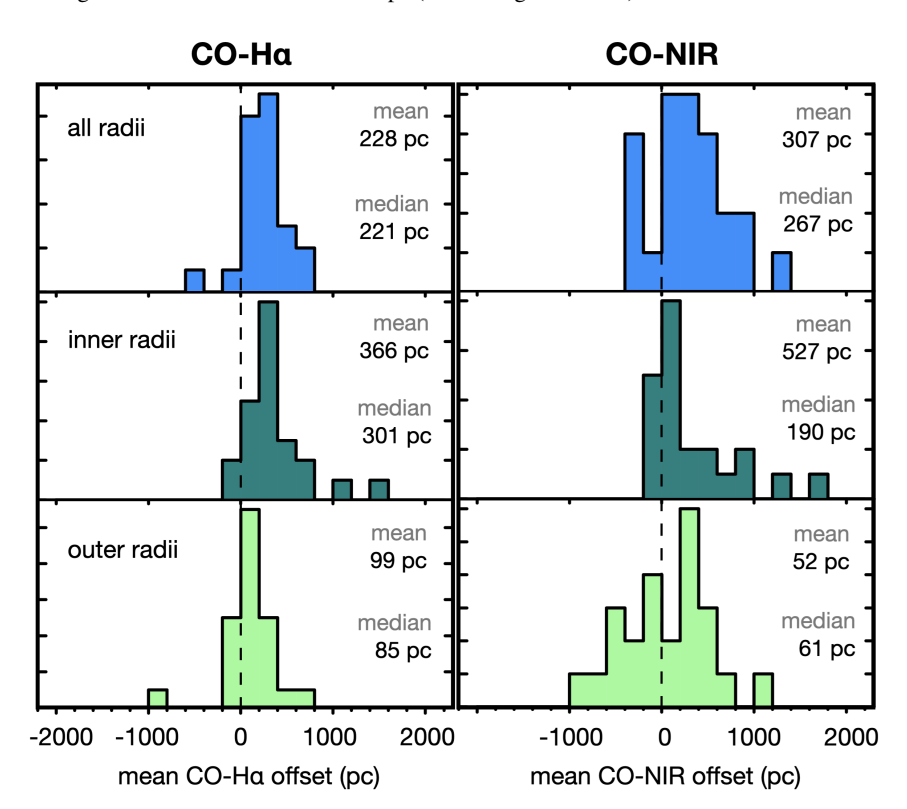


Fig. 4. Histograms showing the distribution of the mean CO-H α and CO-NIR offsets across the whole galaxy sample. Each histogram includes one mean offset per galaxy, computed by averaging all measured offsets for all radii (top), the inner half (middle, $R < (R_{\min}^{\rm CO} + R_{\max}^{\rm CO})/2$), and the outer half (bottom, $R \geq (R_{\min}^{\rm CO} + R_{\min}^{\rm CO})/2$)).

whether offsets decrease with galactocentric radius, in Fig. 4 and Table 1 we also split into the innermost and outermost half radii for each galaxy $(R < (R_{\min}^{\rm CO} + R_{\max}^{\rm CO})/2)$, and $R \ge (R_{\min}^{\rm CO} + R_{\max}^{\rm CO})/2$, respectively). While an arbitrary cut, this division maximises the number of datapoints in two radial bins, which allowed us to check if a radial trend is present despite large scatter. Overall, the mean offsets become closer to zero or even negative from the inner to the outer radii (from an average of 370 pc down to

100 pc). In Sect. 4.2 we examine the radial dependence of offsets in more detail. For completeness, the right panels of Fig. 4 show the offsets between molecular gas and stellar mass peaks (CO-NIR), which follow a similar behaviour as the CO-H α offsets albeit with more scatter; we focus on this in Sect. 4.3.

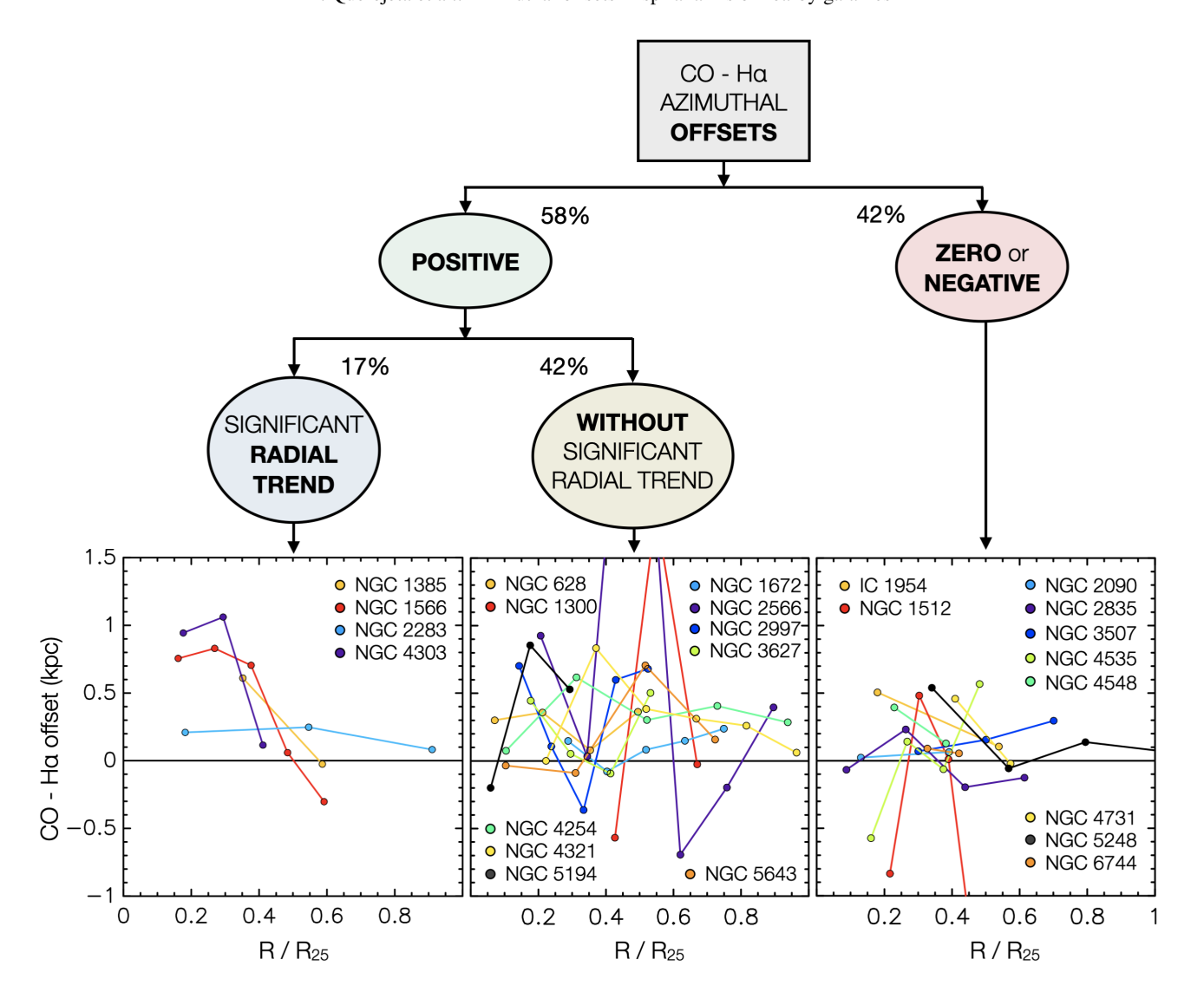


Fig. 5. Classification of galaxies in our sample into three categories depending on whether they show positive mean CO-H α offsets or not and whether there is a significant trend with radius or not. The error bars are smaller than the size of the plotted circles. The solid lines show running means for individual galaxies plotted against radius normalised by R_{25} . All galaxies are barred except for NGC 628, NGC 1385, NGC 2090, NGC 2997, and NGC 4254.

4.2. Radial variation in the offsets

Figure 5 shows the radial behaviour of mean CO-H α offsets for our sample of spiral galaxies. We split them into three groups, depending on whether they show positive mean offsets and a significant radial trend or not. 58% of the galaxies show positive offsets. For the remaining 42% of the galaxies, the offsets are either negative or indistinguishable from zero (we checked if the distribution of offsets within a given galaxy is statistically different from a normal distribution with the same standard deviation randomly distributed around zero offset, with a KS test with a p-value less than 0.05 as the mean over 10 000 runs). These galaxies would be compatible with dynamical (transient) spirals or material arms according to the scenarios outlined in Fig. 2.

Among the galaxies with clear positive mean offsets, four galaxies (17% of the total) also show a significant declining radial trend, with a rank correlation coefficient $\rho < -0.2$ (NGC 1385, NGC 1566, NGC 2283, NGC 4303). In these cases, the left panel of Fig. 5 confirms that the running means generally follow a monotonic declining trend with radius, implying

that these galaxies might be compatible with a quasi-stationary spiral density wave according to the expectations from Fig. 2. In Sect. 4.4 below we derive the pattern speed that would be implied for these galaxies following the method from Egusa et al. (2009).

For the ten remaining galaxies with positive net offsets (42% of the total), the declining radial correlation is very poor or non-existent ($\rho > -0.2$). This less systematic radial behaviour is also manifested by the oscillations in the running means in the middle panel of Fig. 5. For these galaxies, multiple overlapping modes might be present in the disc. For some galaxies, the offsets at certain radii are exceedingly large because at that point the spiral is nearly tangent to the circular bins where we perform the measurements (very low pitch angle); this is the case for NGC 1300, for example. In Sect. 5 we discuss the implications of these findings and caveats in more detail. Fig. B.5 shows the individual offsets as a function of radius for each galaxy.

4.3. Offsets between stellar mass and molecular gas

If we follow Roberts (1969), gas in spiral arms is expected to shock immediately before the potential minimum; thus, CO should peak before the maximum stellar mass surface density, leading to positive CO-NIR offsets inside co-rotation (we trace the potential minimum using a NIR stellar mass map; see Sect. 3.3). However, simulations with a fixed potential show that the position of the shock compared to the potential minimum actually depends on the gas sound speed (Dobbs 2007; Wada 2008). In this context, we may expect more mixed results for CO-NIR offsets than for CO-H α even in the context of quasistationary density wave theory.

Figure 4 shows that CO-NIR offsets also tend to be predominantly positive, in agreement with the classical picture from Roberts (1969). We also find a net decrease in the mean offset when shifting from inner to outer radii. Thus, the study of CO-NIR offsets paints a similar picture as the study of CO-H α offsets. This connection is also confirmed by the fact that despite significant scatter, the individual CO-H α and CO-NIR offsets display a moderate correlation with each other (ρ = 0.43).

Figure 6 shows the distribution of CO-NIR offsets as a function of galactocentric radius in NGC 1566 and NGC 1300. This demonstrates that despite a large scatter, there is a mild radial trend.

Table 1 lists the average azimuthal offsets between CO and H α , as well as between CO and NIR, for each galaxy in our sample. This confirms that despite the bulk mean offsets that we measure, the scatter of individual offset measurements is generally large. The median of the standard deviation in the offsets is ~ 1 kpc. This makes it clear that additional factors come to play in determining the actual local offset for a given location. We discuss this in more detail in Sect. 5.2 below.

Tracing the potential minimum is less straightforward than locating CO or H α peaks (because the stellar mass contrasts are smaller, e.g. Querejeta et al. 2024 and many previous works). To confirm the positive bulk CO-NIR offsets, we repeated the measurements with an alternative tracer, JWST NIRCam F200W instead of the ICA-based stellar mass map. For the galaxies where JWST NIRCam mapping is available, the mean offset is 433 pc for ICA and 291 pc for NIRCam. It is worth noting that there are significant local differences, though, which make it clear that pinpointing the minimum of the gravitational potential within spiral arms is challenging, but the fact that there is a net positive CO-NIR offset within our field-of-view seems robust.

4.4. Deriving star formation timescales and pattern speeds

For the four galaxies where we found positive mean CO-H α offsets and a significant decreasing radial trend ($\rho < -0.2$), namely NGC 1385, NGC 1566, NGC 2283, and NGC 4303, we followed Egusa et al. (2009) to infer the pattern speed and star formation timescales that would be implied by the radial trend of the offsets. We fitted the offsets as a function of $\Omega = v_{\rm rot}/R$ according to Fig. 1 (accounting for the error bars). The resulting fits for the pattern speeds are listed in Table 2, including also fits for each individual spiral arms.

For a few galaxies in our sample, Williams et al. (2021) determined the pattern speed using the Tremaine-Weinberg (TW) method (Tremaine & Weinberg 1984). This method was applied to several tracers (CO, $H\alpha$, and MUSE stellar kinematics), and the conclusion, which agrees with previous expectations, is that the most reliable pattern speeds are those derived applying TW

to MUSE stellar kinematics (confirmed by Borodina et al. 2023 using simulations).

For NGC 1385, Williams et al. (2021) derived $\Omega_{\rm P}=25.0^{+5.6}_{-19.3}\,{\rm km\,s^{-1}\,kpc^{-1}}$ for the stellar TW, which is in excellent agreement with our derived value of $\Omega_{\rm P}=26.1\pm13.8\,{\rm km\,s^{-1}\,kpc^{-1}}$, though the error bars are large in both cases. Our value of $\Omega_{\rm P}=26.1\,{\rm km\,s^{-1}\,kpc^{-1}}$ corresponds to a corotation radius at $R_{\rm CR}=4.8\,{\rm kpc}$.

NGC 1566 is the galaxy that shows the strongest correlation coefficient between CO–H α and Ω in our sample ($\rho\sim0.6$). The implied pattern speed, which is in excellent agreement between both spiral arms, is $25.0\pm4.8\,\mathrm{km\,s^{-1}\,kpc^{-1}}$ (which corresponds to $R_{\rm CR}=7.6\,\mathrm{kpc}$). For NGC 1566, Williams et al. (2021) obtained $\Omega_P=29.4^{+9.1}_{-7.2}\,\mathrm{km\,s^{-1}\,kpc^{-1}}$ for MUSE stellar kinematics, compatible within 1σ with our value. Comte (1983) derived a slightly lower value of $\Omega_P=18.25\,\mathrm{km\,s^{-1}\,kpc^{-1}}$ based on morphology, while Korchagin et al. (2005) obtained $\Omega_P=33\,\mathrm{km\,s^{-1}\,kpc^{-1}}$ comparing with tailored hydrodynamical simulations. Thus, our value lies well within the range spanned by the previous determinations from the literature.

For NGC 2283, Williams et al. (2021) only applied TW to the molecular gas maps (because no MUSE data were available for this galaxy), obtaining $\Omega_P=41.0^{+1.9}_{-3.1}~{\rm km\,s^{-1}\,kpc^{-1}}$. This is significantly larger than our derived value of $\Omega_P=28.2\pm7.0~{\rm km\,s^{-1}\,kpc^{-1}}$; however, as commented above, applying TW to the clumpy gas component cannot be considered as reliable as the measurements based on stellar kinematics (Williams et al. 2021; Borodina et al. 2023).

For NGC 4303, Williams et al. (2021) obtained $\Omega_{\rm P}=43.5^{+5.3}_{-10.0}~{\rm km\,s^{-1}\,kpc^{-1}}$ for MUSE stellar kinematics, which is slightly larger than our determination of $\Omega_{\rm P}=34.8\pm20.1~{\rm km\,s^{-1}\,kpc^{-1}}$ but agrees within 1σ if we consider the significant error bar in this case. For NGC 4303 (as well as for NGC 1385 and NGC 1566), the field of view of the MUSE observations used by Williams et al. (2021) was very similar to the field of view of the PHANGS-ALMA maps used here, which means that both studies focused on the same radial range within the galaxies. Our pattern speed for NGC 4303 implies a corotation radius at $R_{\rm CR}=5.9~{\rm kpc}$. The fact that this is well outside the bar co-rotation radius ($R_{\rm CR}^{\rm bar}=3.4\pm0.2~{\rm kpc}$; Ruiz-García et al. 2024) confirms that the bar and spiral do not rotate with the same pattern speed (i.e. they are not directly coupled).

Table 2 also lists the star formation timescales derived fitting the CO-H α offsets as a function of Ω . They are typically of several megayears (ranging 2–12 Myr for the different galaxies), which broadly agrees with the star formation timescale of a few megayears associated with H α as measured for PHANGS galaxies (e.g. Chevance et al. 2020; Kim et al. 2021, 2022).

5. Discussion

5.1. Do stars and gas cross spiral arms?

As explained in the introduction, theories on the nature of spiral arms can be broadly divided into two main classes. The first class posits that spiral arms are always made up of the same material; they can either be dynamical spirals (transient features which might be self-excited and swing-amplified), or material arms, which are relatively long-lived (possibly tidally induced by an interaction, e.g. Toomre 1969, 1981). A second class encompasses quasi-stationary density waves and, in theory, also kinematic spirals (Kalnajs 1973), where stars and gas flow through the spiral arms (Dobbs & Baba 2014). As explained in Sect. 2,

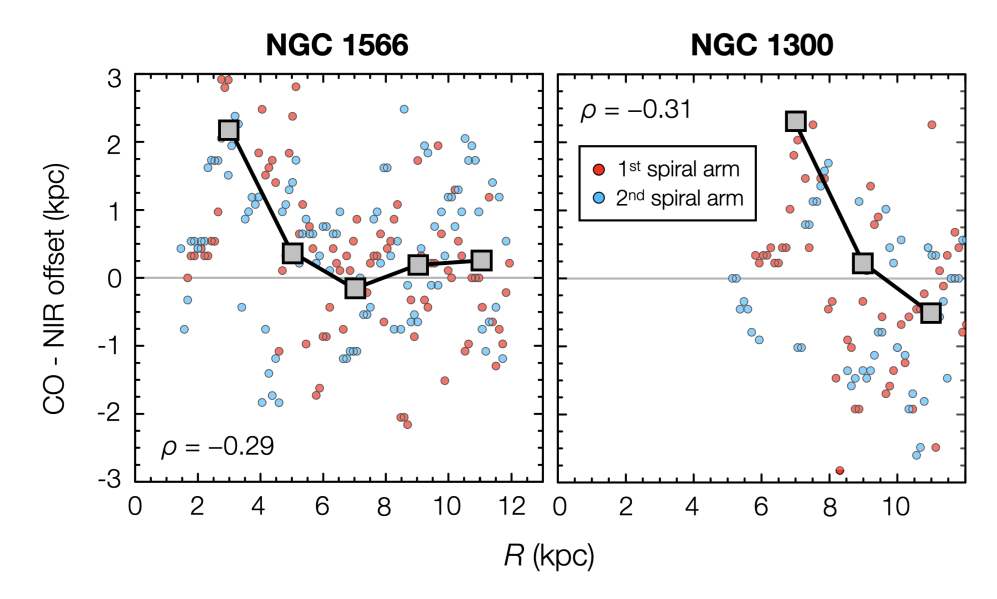


Fig. 6. CO-NIR offsets as a function of galactocentric radius for the galaxies NGC 1566 and NGC 1300. The error bars are comparable to the size of the plotted circles. The ρ value in the corner indicates the strength of the correlation (Spearman rank coefficient).

Table 1. Mean CO-H α and CO-NIR offsets and their scatter.

	$\langle \theta_{\mathrm{CO-H}\alpha} \rangle$	σ	$\langle \theta_{\mathrm{CO-H}\alpha}^{\mathrm{inner}} \rangle$	σ	$\langle \theta_{\mathrm{CO-H}\alpha}^{\mathrm{outer}} \rangle$	σ	$\langle \theta_{\rm CO-NIR} \rangle$	σ	$\langle \theta_{ m CO-NIR}^{ m inner} \rangle$	σ	$\langle \theta_{ m CO-NIR}^{ m outer} \rangle$	σ
IC1954	206*	1040	242*	1029	171*	1062	536	1157	536	717	536*	1469
NGC0628	236	948	343	1223	152	650	220	934	185*	1138	247	739
NGC1300	457	3587	656	4318	278*	2801	526	2728	1660	3506	-485*	1021
NGC1385	265	1040	503	1215	21.8*	767	370*	1272	451*	1344	288*	1205
NGC1512	-402	3083	-9.0*	3761	-916*	1784	990*	4702	2142	5928	-516*	1193
NGC1566	403	1064	750	916	60.1	1094	545	1452	990	1627	105*	1097
NGC1672	106	582	10.0*	789	178	352	184	570	-67.5*	667	372	397
NGC2090	32.5*	596	7.4*	676	56.1*	520	32.2*	798	93.3*	822	-25.1*	783
NGC2283	201	752	411	739	-0.2*	716	64.6	703	179*	739	-45.5*	656
NGC2566	737	5110	1509	6182	78.7	3900	1206	4866	2714	6153	-78.8	2878
NGC2835	-11.3	852	123	997	-181	586	-232	998	-46.7	1131	-466	743
NGC2997	250	2135	199	1244	311	2876	618	1857	194	1052	1133	2420
NGC3507	146*	1757	232*	1622	55.6*	1908	752*	1920	844*	1907	655*	1956
NGC3627	176	962	251	827	83.7*	1107	-154*	1157	-141*	1041	-170 *	1294
NGC4254	377	1093	357	918	410	1344	55.2*	1175	251*	988	-273*	1382
NGC4303	691	2070	1181*	2191	316*	1922	-229*	3911	681*	5244	-925*	2317
NGC4321	409	1738	590	2018	86.1	1018	903	2317	1400	2599	17.4*	1319
NGC4535	0.1	937	-155*	1070	209	680	269*	1112	288*	1062	244*	1189
NGC4548	254*	896	394*	639	128*	1073	-332*	1090	40.9*	672	-665*	1282
NGC4731	188*	575	355*	531	-10.9*	571	193*	965	162*	701	229*	1221
NGC5194	399	1111	29.3*	923	761	1164	335	761	152*	481	516	927
NGC5248	71.8*	798	209	891	-110*	616	-212	656	-117	750	-338	481
NGC5643	282	2114	295	2481	269*	1671	265	2240	160	2663	373	1712
NGC6744	1.2*	1051	307*	1388	-37.5*	1006	457	2770	-98.9*	912	527	2918

Notes. Average azimuthal offsets among tracers (CO and H α , CO and NIR) for each galaxy considering all radial bins, $\langle \theta_{\text{CO-X}} \rangle$, the innermost half of the radial bins, $\langle \theta_{\text{CO-X}}^{\text{outer}} \rangle$, and the outermost half of the radial bins, $\langle \theta_{\text{CO-X}}^{\text{outer}} \rangle$. The σ column next to each average value shows the standard deviation of that distribution. The \star superscript indicates that the distribution of offsets is statistically indistinguishable from a normal distribution with the same standard deviation randomly distributed around zero (KS test with mean p-value greater than 0.05 over 10 000 runs).

offsets can allow us to differentiate between these two major classes of spiral theories.

We examined a set of well-delineated spirals from the PHANGS sample. Despite significant scatter, in 58% of the galaxies we find net positive offsets between CO and $H\alpha$, suggesting that the gas rotates faster than the spiral perturbation (i.e. gas 'overtakes' the spiral). This explains why, on average, young

stars associated with $H\alpha$ are displaced towards the leading side of the spiral (i.e. 'downstream') compared to the maximum accumulation of molecular gas traced by CO. Below in Sect. 5.2 we discuss the implications of the scatter in the offsets.

If we restrict ourselves to the few scenarios introduced in Fig. 2, our observations would support some form of rigidly rotating (though not necessarily long-lived) density wave modes

Table 2. Pattern speed and star formation timescales.

galaxy	arm	ρ	$\Omega_{ m P}$	$\Delta\Omega_{ m P}$	$t_{ m H}\alpha$	$\Delta t_{\mathrm{H}\alpha}$
NGC1385	all	0.31	26.1	13.8	8.96	3.32
NGC1385	sp1	0.25	25.8	18.3	8.92	4.42
NGC1385	sp2	0.36	26.3	21.6	9.00	5.18
NGC1566	all	0.56	25.0	4.8	2.47	0.32
NGC1566	sp1	0.50	24.0	6.0	2.74	0.46
NGC1566	sp2	0.61	26.0	7.0	1.77	0.33
NGC2283	all	0.32	28.2	7.0	1.79	0.29
NGC2283	sp1	0.31	29.9	11.4	4.72	1.20
NGC2283	sp2	0.37	28.0	9.3	1.18	0.25
NGC4303	all	0.40	34.8	20.1	12.27	4.93
NGC4303	sp1	0.25	38.1	65.2	27.39	32.76
NGC4303	sp2	0.46	32.9	12.8	5.15	1.41

Notes. ρ is the strength of the correlations of θ (deg) vs Ω (km s⁻¹ kpc⁻¹), and the implied pattern speed and star formation timescale following Egusa et al. (2009) for the four galaxies with mean positive offsets and a significant radial trend. 'sp1' and 'sp2' denote the fits for individual spiral arms, whereas 'all' lists the fits for all spiral arms in a given galaxy simultaneously. Pattern speeds are in units of km s⁻¹ kpc⁻¹ and star formation timescale are in units of Myr.

for nearly two-thirds of the sample. The net positive offsets that we measure per galaxy are typically ~200-300 pc in the plane of the galaxy. This is consistent with the displacement expected within a timescale of a few megayears. Indeed, for example, for a radius of $R \sim 5$ kpc, a representative rotation curve of $v_{\rm rot} \sim 150\,{\rm km~s^{-1}}$ (Lang et al. 2020), and a reasonable pattern speed of $\Omega_{\rm P} \sim 20\,{\rm km~s^{-1}}$ kpc⁻¹, an offset of 200–300 pc corresponds to a timescale of $\sim 4-6\,{\rm Myr}$, which matches the star formation timescales inferred for PHANGS galaxies using $H\alpha$ as a star formation tracer (e.g. Chevance et al. 2020; Kim et al. 2021, 2022). Therefore, a priori, the magnitude of the offsets seems roughly consistent with the expectation for a representative rotation curve and a reasonable spiral pattern speed. Yet, it is important to emphasise that while we use gas and young stars as tracers, this does not imply that a density wave is sustained in the gaseous disc (which is sensitive to complex hydrodynamical and feedback effects); gas might just be locally responding to an underlying spiral density wave present in the old stellar population (which would agree with the modest but clearly positive Σ_{\star} arm/interarm contrasts found by Querejeta et al. 2024). The typical mean offset of 200-300 pc per galaxy corresponds to an angular offset of 5-7" for our nearest targets ($d \sim 9 \,\mathrm{Mpc}$) and 2-3'' for the most distant ones ($d \sim 23$ Mpc); this could explain why some previous studies with coarser resolution did not detect significant offsets, especially for the most distant galaxies.

For 42% of the galaxies, we find CO-H α offsets which are indistinguishable from zero or even negative. In these cases, it is possible that gas and stars are actually co-rotating with the spiral perturbation, without crossing the arms. At least two mechanisms can explain this scenario: dynamic spirals which can appear in isolated discs and material arms which can be tidally excited by the passage of a companion galaxy. The former consist of local hydrodynamical perturbations which are swing-amplified and sheared into spiral segments as a consequence of differential rotation; these are commonly found in hydrodynamical simulations (e.g. Sellwood & Carlberg 1984, 2014; D'Onghia et al. 2013; Pettitt et al. 2015, 2020; Durán-Camacho et al. 2024). On the other hand, material arms can be long and coherent, potentially tidally dragged by a companion

during an interaction. The fact that these galaxies show positive Σ_{\star} arm/interarm contrasts (Querejeta et al. 2024) would argue in favour of material arms as opposed to shorter transient spirals, which would not necessarily stand out in the old stellar component.

In principle, if we sample well beyond co-rotation a galaxy with a single quasi-stationary spiral density wave, the average offset could be zero (because positive offsets inside co-rotation could compensate negative offsets outside). However, this possibility is ruled out by Fig. 5 because we did not find any galaxies with zero mean offsets where running means monotonically decrease from positive to negative as radius increases. In any case, the limited PHANGS-ALMA fields of view might be obscuring this (see Sect. 5.4).

Following the spiral family nomenclature from Elmegreen (1990), our galaxy sample is made up of 15 grand-design, seven multi-armed, and two flocculent spirals (following Buta et al. 2015 and Meidt et al. 2021, as listed in Querejeta et al. 2024; see Table A.1). One could perhaps expect a higher proportion of grand-design spirals within the group of galaxies with positive offsets and a clear trend, compatible with a quasi-stationary density wave. Interestingly, this is not the case, and among the four galaxies in that group, only one is grand-design; perhaps even more surprisingly, both flocculent spirals (NGC 1385 and NGC 2283) fall into this category. This questions the widespread idea that grand-design spirals are generally associated with quasi-stationary density waves while flocculent spirals are made up of transient, dynamic spirals (Dobbs & Baba 2014). It is worth noting that none of the galaxies in this first group seems to be interacting; galaxies with clear signs of interaction either show positive offsets without a clear radial trend, which might be evidence of multiple modes (e.g. NGC 3627, NGC 4321, NGC 5194), or they do not show net positive offsets at all, which would agree with material arms driven by the interaction (NGC 1512, NGC 4731). In any case, none of these galaxies are evolved ongoing mergers comparable to the Antennae; they are interacting pairs, typically separated by distances of ~100 kpc or more. The only case of a closely interacting pair is M51 (NGC 5194), and, to a lesser extent, NGC 1512.

In addition to galaxy interactions, bars have also been argued to have the ability to induce spiral arms (e.g. Sanders & Huntley 1976; Sellwood & Sparke 1988; Block et al. 2004; Athanassoula et al. 2010; Salo et al. 2010). Our sample is overall clearly biased towards barred galaxies, since as many as 19 out of 24 galaxies (79%) are barred according to Querejeta et al. (2021). Except for NGC 1385, all four galaxies with positive offsets and a clear radial trend have a large-scale bar. In the remaining categories of mean positive offsets without a clear radial trend and zero or negative mean offsets, we find a fraction of 70% and 90% barred galaxies. Thus, the presence of a bar alone cannot explain the differences we found.

In some grand-design spiral galaxies it has been suggested that a certain radial range behaves as a quasi-stationary density wave, while at other radii it can have a material nature (e.g. in M51; Colombo et al. 2014; Chandar et al. 2017). The same might apply to other interacting galaxies, some of which are clearly asymmetric (e.g. NGC 3627). As we are mostly sampling the inner part of galaxies, if the inner part behaves as quasi-stationary density wave and the outer one as material arms (as often argued for M51), we would be exclusively sensitive to the inner behaviour. Thus, our results cannot be necessarily extrapolated to the entire galaxy. Also, in principle interactions could induce asymmetries, which may result in a given arm behaving differently from another arm. For this reason, we examine

the radial trend of the offsets for each spiral arm independently. Indeed, Egusa et al. (2009) also found differences among spiral arms within certain galaxies. Inspecting Fig. B.5 in the Appendix, as well as the corresponding correlation coefficients, we conclude that in most cases the behaviour of one arm is closely mirrored by the second or third arm.

Spiral arms are often recognised as a source of large-scale azimuthal metallicity variations. Some studies identified significant metallicity differences in spiral arms (e.g. Ho et al. 2017, 2018), and even more so for grand-design spirals (Sánchez-Menguiano et al. 2020); yet, other studies did not find clear trends associated with spiral arms (Williams et al. 2022a) or did so only for some galaxies (Kreckel et al. 2019). In this context, recent numerical simulations point to the prerequisite of a radial metallicity gradient, which can then lead to azimuthal metallicity variations as a result of radial gas flows driven by spiral arms (Khoperskov et al. 2023; Orr et al. 2023). Chen et al. (2024) examined gas-phase metallicity variations in nine spiral galaxies, with strong evidence supporting quasi-stationary density wave in NGC 1566 (and not in NGC 2835 or NGC 6744), in agreement with our findings. While no correlations between our results and the azimuthal patterns presented in eight galaxies in Kreckel et al. (2019) are apparent, detailed constraints on the different spiral mechanisms acting in specific galaxies could provide a novel constraint on models, and may aid our understanding of the role spiral arms play in mixing the ISM and driving patterns in the gas-phase abundances.

5.2. Star formation is not uniquely initiated at a spiral shock

As explained in Sect. 2, previous observations demonstrated that star formation in spiral galaxies is not exclusively triggered at the spiral shock. As expected, this results in a large scatter among the azimuthal offsets. While the mean offsets that we measure in our sample are typically of a few hundred parsecs, the scatter of the offsets is of the order of ~ 1 kpc (Table 1).

The large scatter is partially a result of the high resolution of our observations, which reflects local conditions and small-scale physics effects. With our improved resolution compared to previous studies, we start resolving individual clouds and star forming complexes, at scales where star formation is subject to stochastic sampling effects (e.g. Schruba et al. 2010). Gravitational instabilities and local turbulence triggered by supernova bubbles (and other forms of stellar feedback) also play a role in shaping the interstellar medium on small scales, and it can regulate its ability to produce new stars. Specifically, we know that much star formation in spiral arms is not confined to a spiral shock, but taking place in spur- and feather-like gas structures (e.g. La Vigne et al. 2006; Schinnerer et al. 2017; Williams et al. 2022b).

More generally, star formation is not limited to spiral regions, and in absolute terms (total SFR, not Σ_{SFR}) almost as much star formation takes place in interarm regions as in spiral arms (Foyle et al. 2010; Querejeta et al. 2024). This means that mechanisms other than only spiral arms must initiate the collapse of molecular clouds to form stars. Thus at any location relative to the arms, there will be a mixture of gas and star formation related to both processes, and this naturally injects scatter into the offset measurement. In this context, the scatter in our measurements implies that star formation is not uniquely initiated at a coherent spiral shock.

5.3. Are observations consistent with a single pattern speed?

In the framework of quasi-stationary density wave theory, if the entire spiral perturbation rotates as a rigid body (with a single pattern speed), according to Fig. 2 we would expect mean positive offsets in the inner regions of the galaxy and a declining radial trend. The confirmation that a single pattern speed applies throughout the disc would be given by the observation of negative offsets after the co-rotation radius. This condition including negative offsets after a certain radius is only met by NGC 1566. In three more galaxies (NGC 1385, NGC 2283, and NGC 4303), we find a significant decreasing radial trend ($\rho < -0.2$), but the running means do not become negative (Fig. 5), probably because the PHANGS-ALMA field of view does not cover sufficiently large radii, i.e. it likely samples close to, but not beyond the co-rotation radius of the spiral (as shown in Fig. 5 with radii normalised by R_{25}). Yet, if we sampled further out, offsets might become larger again, as a consequence of multiple modes dominating at different radial ranges (predicted for groove modes and in the theory of mode coupling; e.g. Sygnet et al. 1988; Masset & Tagger 1997; Sellwood & Carlberg 2014). Therefore, at least one and up to four galaxies in our sample seem compatible with a single pattern speed.

Another point that adds confidence to these results is the fact that the pattern speeds that we derived in Sect. 4.4 for the four galaxies with a clear radial trend agree well with previous measurements from the literature. These previous studies relied on totally independent methods such as Tremaine-Weinberg applied on stellar kinematics from MUSE (Williams et al. 2021). The star-formation timescales implied by the fitting of the offsets as a function of Ω following Egusa et al. (2009) are of the order of several megayears, which also roughly agrees with independent empirical estimates (e.g. Chevance et al. 2020; Kim et al. 2021, 2022).

For galaxies with positive mean offsets but no clear overall radial trend, several pattern speeds might be at play in the spiral structure. This is expected in the context of the theory of mode coupling (e.g. Sygnet et al. 1988; Masset & Tagger 1997). Simulations such as Rautiainen & Salo (1999) and Roškar et al. (2012) found evidence of multiple pattern speeds in simulations of isolated spiral galaxies. Empirically, multiple pattern speeds have been identified for some galaxies, for example by Meidt et al. (2008, 2009) and Font et al. (2014). Kostiuk et al. (2024) compiled measurements of co-rotation radii from the literature for hundreds of galaxies, based on different methods, and found them to be inconsistent for most galaxies and interpret this as evidence of either multiple spiral modes rotating at different angular velocities or transient spirals. Our sample does not have any galaxies in common with Meidt et al. (2009), but Meidt et al. (2008) and Font et al. (2024) found evidence of several spiral modes in M51 (NGC 5194), which would agree with the fact that we find a net positive CO-H α offset but no consistent radial trend in this galaxy. Several previous studies did not find evidence supporting the (quasi-stationary) density wave nature of the grand-design spiral NGC 4321 (Egusa et al. 2009; Ferreras et al. 2012; Kostiuk et al. 2025); in this case, our analysis of CO- $H\alpha$ offsets points to the existence of multiple modes. The only galaxy in common between our sample and Font et al. (2014) is NGC 4303, for which they found as many as six co-rotation radii (including both bar and spiral); the strongest peak in the Font-Beckman method is located at $R_{\rm CR} = 49.9^{\prime\prime}$, corresponding to $\Omega_P=39\,\mathrm{km\,s^{-1}\,kpc^{-1}}$, which is well compatible with our result of $\Omega_P=34.8\,\mathrm{km\,s^{-1}\,kpc^{-1}}$ based on the fitting of CO-H α

5.4. Robustness of results and caveats

Our offset measurements rely on galactocentric radial bins, which implicitly assume circular trajectories for gas and stars. However, stellar orbits in a real non-axisymmetric two-armed spiral potential are rather elliptical and elongated in the direction of the m = 2 perturbation at each radius (therefore, precessing with radius). This means that if there is a systematic displacement between gas and star formation along the orbit, that distance will be underestimated by our circular bins, especially for more open spirals (large pitch angle) with strong stellar arm/interarm contrasts. However, this does not change the fact that offsets should be positive inside co-rotation and negative outside, flipping sign precisely at co-rotation. Thus, the simple picture that we have painted in the previous sections should remain qualitatively valid, but the detailed numerical results could be affected by this limitation. In terms of fitting pattern speeds following Egusa et al. (2009), we expect the choice of circular sampling to have a stronger impact on the derivation of star formation timescales (which depend on the slope of the fitted line) than the pattern speed (which depends on the intercept), as long as our measurements have a good sampling around co-rotation, where the offsets are expected to be zero and flip their sign.

Since we focus on offsets in the plane of the galaxy, our measurements will be affected by errors in the determination of the inclination and position angle of the disc. Fortunately, for PHANGS galaxies we count on reliable kinematic estimates of these orientation parameters (Lang et al. 2020). We find that perturbing the orientation parameters within their error bars has a typical impact on the offsets and correlation coefficients of at most a few multiples of 10%, and importantly, it does not significantly wash out any radial trends.

Following Egusa et al. (2009), we measured the azimuthal offsets between CO and $H\alpha$ peaks at each radius. In order to assess the robustness of this approach, in Appendix B we also considered the impact of choosing the second brightest azimuthal bin in CO and $H\alpha$ at each radius or the mean position weighted by CO or $H\alpha$ intensity. While individual offset measurements change significantly, our conclusions are not qualitatively affected when adopting either of these alternatives. We also checked how adopting wider radial bins ($\Delta R = 300\,\mathrm{pc}$) affects the offsets and correlation coefficients with radius, but reassuringly, these only change at the level of a few percent.

Another methodological detail that might be questionable is the choice of $H\alpha$ to trace recent star formation, as this optical tracer is known to suffer from severe extinction. While this is true, we are interested in a tracer that emerges after a delay following the onset of star formation, i.e. we aim to 'clock' the time between the collapse of molecular gas and the appearance of young exposed stars that emit in $H\alpha$, which makes this an appropriate tracer. However, dust extinction could be stronger in 'upstream' locations compared to 'downstream' regions (due to higher gas column densities), and it could also be stronger near the centres of the galaxies. This could lead to stronger CO- $H\alpha$ offsets as a function of radius. Yet, as the contribution of these effects should vary monotonically with radius, we would not expect this caveat to limit our ability to distinguish between galaxies with globally positive or zero CO-H α offsets, and it should not prevent us from identifying present radial trends (but the slope of the radial trend would be affected, and therefore the implied star formation timescales could certainly be over- or un-

Another related problem could be associated with changing star formation timescales (see e.g. Schinnerer & Leroy 2024), which could make the radial behaviour more erratic. Specifically, density and other factors affect the time for a star-forming cloud to collapse and form stars (e.g. Sun et al. 2022; Neumann et al. 2023). In particular, Kim et al. (2022) found star formation timescales associated with H α that vary in the range from \sim 5 Myr to \sim 10 Myr for PHANGS galaxies.

It is worth noting that even in the framework of quasistationary density wave theory, the mean measured offset for a given galaxy will depend on the field of view. If our maps only sample the innermost regions, the mean offset will be larger, as the difference between $v_{\rm gas} = \Omega_{\rm gas} R$ and $v_{\rm spiral} = \Omega_{\rm P} R$ increases with decreasing radius. This can explain why the mean offset is so large for galaxies such as NGC 2566 ($\langle \theta_{\rm CO-H\alpha} \rangle = 740 \, \rm pc$), where our ALMA map samples the whole bar but only the beginning of the spiral structure. Fig. 5 allows one to assess this limitation visually, as it displays the running means as a function of R/R_{25} ; in most galaxies we sampled out to ~0.5 R_{25} , with a few CO maps extending further out ($\sim 0.8-0.9R_{25}$). The limited field of view also affects our ability to test whether offsets indeed become negative after a certain radius, as we commented on in Sect. 5.3. This emphasises the importance of wide-field CO mapping for studies such as this one.

6. Summary and conclusions

Spiral arms are some of the most compelling features in nearby disc galaxies, but from a dynamical point of view, their nature remains an open question. Azimuthal offsets between molecular gas and star formation can inform us about the nature of the underlying spiral perturbation. Here we have examined a sample of 24 spiral galaxies from the PHANGS survey with a well-delineated spiral structure, quantifying the offsets between CO and $H\alpha$ peaks within spiral regions in radial bins. Our main findings are as follows:

- Offsets exhibit substantial scatter, supporting previous findings that star formation is not exclusively initiated at the spiral shock (Table 1). Star formation off spiral arms, gravitational instabilities giving rise to spurs and feathers, and turbulence and stellar feedback likely play roles in setting this large scatter among the measured offsets.
- 2. Most galaxies exhibit positive CO-Hα and CO-NIR offsets, typically of a few hundred parsecs (Fig. 4). This corresponds to a star formation timescale of several megayears for a characteristic radius, rotation curve, and spiral pattern speed, which is consistent with previous observations.
- 3. In four galaxies (17%), we find positive mean offsets and a clear radial trend (Fig. 5). This agrees with the expectation for a quasi-stationary spiral density wave with a single pattern speed. For ten galaxies (42%), the mean offset is positive, but there is not such a clear radial trend, which could suggest the superposition of several modes (such that a spiral mode might not develop beyond its own co-rotation). Yet, we caution that field of view limitations complicate the interpretation of these measurements.
- 4. In the remaining ten galaxies (42%), we did not find significant positive offsets (Fig. 5). This would be compatible with transient, dynamical spirals and with material arms possibly dragged by the interaction with a companion. Under either of these scenarios, gas and stars do not overtake the spiral perturbation (i.e. all radii are co-rotating).
- 5. For the four galaxies with clear offsets and a radial trend, we derived pattern speeds in good agreement with the literature (Table 2).

In summary, our results suggest that even well-delineated spirals in the local Universe exhibit significantly different behaviours in terms of CO-H α offsets and their radial distribution. This points to the idea that different kinds of mechanisms are probably responsible for sustaining their spiral structure.

Acknowledgements. This work was carried out as part of the PHANGS collaboration. We would like to thank the anonymous referee for constructive comments that helped us improve the manuscript. MQ, SGB, MRG, MJJD and AU acknowledge support from the Spanish grant PID2022-138560NB-I00, funded by MCIN/AEI/10.13039/501100011033/FEDER, EU. HAP acknowledges support from the National Science and Technology Council of Taiwan under grant 113-2112-M-032-014-MY3. KK acknowledges support from the Deutsche Forschungsgemeinschaft (DFG, German Research Foundation) in the form of an Emmy Noether Research Group (grant number KR4598/2-1, PI Kreckel) and the European Research Council's starting grant ERC StG-101077573 FP acknowledges support from the Horizon Europe (ISM-METALS). FP acknowledges support from the Horizon Europe research and innovation programme under the Maria Skłodowska-Curie grant "TraNSLate" No 101108180, and from the Agencia Estatal de Investigación del Ministerio de Ciencia e Innovación (MCIN/AEI/10.13039/501100011033) under grant (PID2021-128131NB-I00) and the European Regional Development Fund (ERDF) "A way of making Europe". MQ acknowledges discussions with John Beckman and Sim Dlamini. MB acknowledges support from the ANID BASAL project FB210003. This work was supported by the French government through the France 2030 investment plan managed by the National Research Agency (ANR), as part of the Initiative of Excellence of Université Côte d'Azur under reference number ANR-15-IDEX-01. RSK acknowledges financial support from the ERC via Synergy Grant "ECOGAL" (project ID 855130), from the German Excellence Strategy via the Heidelberg Cluster "STRUCTURES" (EXC 2181 - 390900948), and from the German Ministry for Economic Affairs and Climate Action in project "MAINN" (funding ID 50002206). RSK also thanks the 2024/25 Class of Harvard Radcliffe Fellows for highly interesting and stimulating discussions. This work is based on observations and archival data obtained with the *Spitzer* Space Telescope, which is operated by the Jet Propulsion Laboratory, California Institute of Technology under a contract with NASA. This paper makes use of the following ALMA data: ADS/JAO.ALMA#2012.1.00650.S, ADS/JAO.ALMA#2013.1.01161.S, ADS/JAO.ALMA#2015.1.00121.S, ADS/JAO.ALMA#2015.1.00782.S, ADS/JAO.ALMA#2015.1.00925.S, ADS/JAO.ALMA#2015.1.00956.S, ADS/JAO.ALMA#2016.1.00386.S, ADS/JAO.ALMA#2017.1.00886.L, ADS/JAO.ALMA#2018.1.01651.S. ALMA is a partnership of ESO (representing its member states), NSF (USA) and NINS (Japan), together with NRC (Canada), MOST and ASIAA (Taiwan), and KASI (Republic of Korea), in cooperation with the Republic of Chile. The Joint ALMA Observatory is operated by ESO, AUI/NRAO and NAOJ. The National Radio Astronomy Observatory is a facility of the National Science Foundation operated under cooperative agreement by Associated Universities, Inc.

References

Abdeen, S., Kennefick, D., Kennefick, J., et al. 2020, MNRAS, 496, 1610 Anand, G. S., Lee, J. C., Van Dyk, S. D., et al. 2021, MNRAS, 501, 3621 Athanassoula, E., Romero-Gómez, M., Bosma, A., & Masdemont, J. J. 2010, MNRAS, 407, 1433

Baba, J., Morokuma-Matsui, K., & Egusa, F. 2015, PASJ, 67, L4

Bertin, G. 2000, Dynamics of Galaxies

Bertin, G., Lin, C. C., Lowe, S. A., & Thurstans, R. P. 1989, ApJ, 338, 78 Binney, J. 2020, MNRAS, 496, 767

Block, D. L., Buta, R., Knapen, J. H., et al. 2004, AJ, 128, 183

Borodina, O., Williams, T. G., Sormani, M. C., Meidt, S., & Schinnerer, E. 2023, MNRAS, 524, 3437

Buta, R. J., Sheth, K., Athanassoula, E., et al. 2015, ApJS, 217, 32

Cedrés, B., Cepa, J., Bongiovanni, Á., et al. 2013, A&A, 560, A59 Chandar, R., Chien, L. H., Meidt, S., et al. 2017, ApJ, 845, 78

Chen, Q.-H., Grasha, K., Battisti, A. J., et al. 2024, MNRAS, 534, 883

Chevance, M., Kruijssen, J. M. D., Hygate, A. P. S., et al. 2020, MNRAS, 493,

Choi, Y., Dalcanton, J. J., Williams, B. F., et al. 2015, ApJ, 810, 9

Colman, T., Hennebelle, P., Brucy, N., et al. 2025, arXiv e-prints, arXiv:2503.03305

Colombo, D., Meidt, S. E., Schinnerer, E., et al. 2014, ApJ, 784, 4

Comte, G. 1983, in IAU Symposium, Vol. 100, Internal Kinematics and Dynamics of Galaxies, ed. E. Athanassoula, 151

de Vaucouleurs, G., de Vaucouleurs, A., Corwin, Jr., H. G., et al. 1991, Third Reference Catalogue of Bright Galaxies. Volume I: Explanations and references. Volume II: Data for galaxies between 0^h and 12^h . Volume III: Data for galaxies between 12^h and 24^h .

Dobbs, C. 2007, PhD thesis, -

Dobbs, C. & Baba, J. 2014, PASA, 31, e035

Dobbs, C. L. & Bonnell, I. A. 2007, MNRAS, 376, 1747

D'Onghia, E., Vogelsberger, M., & Hernquist, L. 2013, ApJ, 766, 34

Donner, K. J. & Thomasson, M. 1994, A&A, 290, 785

Durán-Camacho, E., Duarte-Cabral, A., Pettitt, A. R., et al. 2024, MNRAS, 532,

Egusa, F., Kohno, K., Sofue, Y., Nakanishi, H., & Komugi, S. 2009, ApJ, 697, 1870

Egusa, F., Mentuch Cooper, E., Koda, J., & Baba, J. 2017, MNRAS, 465, 460 Elmegreen, B. G. 1990, Annals of the New York Academy of Sciences, 596, 40 Federrath, C. 2015, MNRAS, 450, 4035

Ferreras, I., Cropper, M., Kawata, D., Page, M., & Hoversten, E. A. 2012, MN-RAS, 424, 1636

Font, J., Beckman, J. E., Epinat, B., Dobbs, C. L., & Querejeta, M. 2024, ApJ, 966, 110

Font, J., Beckman, J. E., Epinat, B., et al. 2011, ApJ, 741, L14

Font, J., Beckman, J. E., Querejeta, M., et al. 2014, ApJS, 210, 2

Foyle, K., Rix, H. W., Dobbs, C. L., Leroy, A. K., & Walter, F. 2011, ApJ, 735,

Foyle, K., Rix, H. W., Walter, F., & Leroy, A. K. 2010, ApJ, 725, 534 Garcia-Burillo, S., Combes, F., & Gerin, M. 1993, A&A, 274, 148

Gittins, D. M. & Clarke, C. J. 2004, MNRAS, 349, 909

Goldreich, P. & Lynden-Bell, D. 1965, MNRAS, 130, 125

Grand, R. J. J., Kawata, D., & Cropper, M. 2012a, MNRAS, 426, 167

Grand, R. J. J., Kawata, D., & Cropper, M. 2012b, MNRAS, 421, 1529 Grosbøl, P. & Dottori, H. 2009, A&A, 499, L21

Hamilton, C. 2024, MNRAS, 528, 5286

Herrera-Endoqui, M., Díaz-García, S., Laurikainen, E., & Salo, H. 2015, A&A, 582, A86

Ho, I. T., Meidt, S. E., Kudritzki, R.-P., et al. 2018, A&A, 618, A64

Ho, I. T., Seibert, M., Meidt, S. E., et al. 2017, ApJ, 846, 39

Julian, W. H. & Toomre, A. 1966, ApJ, 146, 810

Kalnajs, A. J. 1973, PASA, 2, 174

Kawata, D., Hunt, J. A. S., Grand, R. J. J., Pasetto, S., & Cropper, M. 2014, MNRAS, 443, 2757

Khoperskov, S., Sivkova, E., Saburova, A., et al. 2023, A&A, 671, A56

Kim, J., Chevance, M., Kruijssen, J. M. D., et al. 2022, MNRAS, 516, 3006 Kim, J., Chevance, M., Kruijssen, J. M. D., et al. 2021, MNRAS, 504, 487

Korchagin, V., Orlova, N., Kikuchi, N., Miyama, S. M., & Moiseev, A. V. 2005, arXiv e-prints, astro

Kostiuk, V., Marchuk, A., Gusev, A., & Chugunov, I. V. 2025, Galaxies, 13, 27 Kostiuk, V. S., Marchuk, A. A., & Gusev, A. S. 2024, Research in Astronomy and Astrophysics, 24, 075007

Kreckel, K., Ho, I. T., Blanc, G. A., et al. 2019, ApJ, 887, 80 Krumholz, M. R. 2015, ArXiv e-prints

La Vigne, M. A., Vogel, S. N., & Ostriker, E. C. 2006, ApJ, 650, 818

Lang, P., Meidt, S. E., Rosolowsky, E., et al. 2020, ApJ, 897, 122

Lee, J. C., Sandstrom, K. M., Leroy, A. K., et al. 2023, ApJ, 944, L17

Leroy, A. K., Hughes, A., Liu, D., et al. 2021a, ApJS, 255, 19

Leroy, A. K., Sandstrom, K. M., Lang, D., et al. 2019, ApJS, 244, 24

Leroy, A. K., Schinnerer, E., Hughes, A., et al. 2021b, ApJS, 257, 43 Lin, C. C. & Shu, F. H. 1964, ApJ, 140, 646

Lin, C. C. & Shu, F. H. 1966, Proceedings of the National Academy of Science, 55, 229

Louie, M., Koda, J., & Egusa, F. 2013, ApJ, 763, 94

Marchuk, A. A. 2024, A&A, 686, L14

Marchuk, A. A., Chugunov, I. V., Gontcharov, G. A., et al. 2024a, MNRAS, 528, 1276

Marchuk, A. A., Mosenkov, A. V., Chugunov, I. V., et al. 2024b, MNRAS, 527,

Martínez-García, E. E. & González-Lópezlira, R. A. 2013, ApJ, 765, 105 Martínez-García, E. E., González-Lópezlira, R. A., & Puerari, I. 2023, MNRAS,

Masset, F. & Tagger, M. 1997, A&A, 322, 442

Meidt, S. E., Leroy, A. K., Querejeta, M., et al. 2021, ApJ, 913, 113

Meidt, S. E., Rand, R. J., & Merrifield, M. R. 2009, ApJ, 702, 277

Meidt, S. E., Rand, R. J., Merrifield, M. R., Shetty, R., & Vogel, S. N. 2008, ApJ, 688, 224

Meidt, S. E., Schinnerer, E., Knapen, J. H., et al. 2012, ApJ, 744, 17

Meidt, S. E., Schinnerer, E., van de Ven, G., et al. 2014, ApJ, 788, 144

Meidt, S. E. & van der Wel, A. 2024, ApJ, 966, 62

Miller, R., Kennefick, D., Kennefick, J., et al. 2019, ApJ, 874, 177

Nair, P. B. & Abraham, R. G. 2010, ApJS, 186, 427

Neumann, L., Gallagher, M. J., Bigiel, F., et al. 2023, MNRAS, 521, 3348

Orr, M. E., Burkhart, B., Wetzel, A., et al. 2023, MNRAS, 521, 3708

Pan, H.-A., Schinnerer, E., Hughes, A., et al. 2022, ApJ, 927, 9

Peterken, T. G., Merrifield, M. R., Aragón-Salamanca, A., et al. 2019, Nature Astronomy, 3, 178

Pettitt, A. R., Dobbs, C. L., Acreman, D. M., & Bate, M. R. 2015, MNRAS, 449,

Pettitt, A. R., Dobbs, C. L., Baba, J., et al. 2020, MNRAS, 498, 1159

Pety, J., Schinnerer, E., Leroy, A. K., et al. 2013, ApJ, 779, 43 Querejeta, M., Leroy, A. K., Meidt, S. E., et al. 2024, A&A, 687, A293 Querejeta, M., Meidt, S. E., Schinnerer, E., et al. 2015, ApJS, 219, 5 Querejeta, M., Schinnerer, E., Meidt, S., et al. 2021, A&A, 656, A133 Rautiainen, P. & Salo, H. 1999, A&A, 348, 737 Roberts, W. W., J., Roberts, M. S., & Shu, F. H. 1975, ApJ, 196, 381

Roberts, W. W. 1969, ApJ, 158, 123 Roškar, R., Debattista, V. P., Quinn, T. R., & Wadsley, J. 2012, MNRAS, 426,

2089 Ruiz-García, M., Querejeta, M., García-Burillo, S., et al. 2024, A&A, 691, A351

Salim, S., Boquien, M., & Lee, J. C. 2018, ApJ, 859, 11 Salim, S., Lee, J. C., Janowiecki, S., et al. 2016, ApJS, 227, 2

Salo, H., Laurikainen, E., Buta, R., & Knapen, J. H. 2010, ApJ, 715, L56 Sánchez-Menguiano, L., Sánchez, S. F., Pérez, I., et al. 2020, MNRAS, 492,

4149

Sanders, R. H. & Huntley, J. M. 1976, ApJ, 209, 53

Schinnerer, E. & Leroy, A. K. 2024, ARA&A, 62, 369

Schinnerer, E., Meidt, S. E., Colombo, D., et al. 2017, ApJ, 836, 62

Schinnerer, E., Meidt, S. E., Pety, J., et al. 2013, ApJ, 779, 42

Schruba, A., Leroy, A. K., Walter, F., Sandstrom, K., & Rosolowsky, E. 2010, ApJ, 722, 1699

Sellwood, J. A. & Carlberg, R. G. 1984, ApJ, 282, 61

Sellwood, J. A. & Carlberg, R. G. 2014, ApJ, 785, 137

Sellwood, J. A. & Masters, K. L. 2022, ARA&A, 60

Sellwood, J. A. & Sparke, L. S. 1988, MNRAS, 231, 25P

Shabani, F., Grebel, E. K., Pasquali, A., et al. 2018, MNRAS, 478, 3590

Sheth, K., Regan, M., Hinz, J. L., et al. 2010, PASP, 122, 1397 Sridhar, S. 2019, ApJ, 884, 3

Sun, B., Calzetti, D., & Battisti, A. J. 2024, ApJ, 973, 137

Sun, J., Leroy, A. K., Ostriker, E. C., et al. 2020, ApJ, 892, 148 Sun, J., Leroy, A. K., Rosolowsky, E., et al. 2022, AJ, 164, 43

Sygnet, J. F., Tagger, M., Athanassoula, E., & Pellat, R. 1988, MNRAS, 232, 733

Tamburro, D., Rix, H. W., Walter, F., et al. 2008, AJ, 136, 2872 Toomre, A. 1969, ApJ, 158, 899

Toomre, A. 1981, in Structure and Evolution of Normal Galaxies, ed. S. M. Fall & D. Lvnden-Bell, 111-136

Tremaine, S. & Weinberg, M. D. 1984, ApJ, 282, L5

Tress, R. G., Smith, R. J., Sormani, M. C., et al. 2020, MNRAS, 492, 2973

Vogel, S. N., Kulkarni, S. R., & Scoville, N. Z. 1988, at, 334, 402

Wada, K. 2008, ApJ, 675, 188

Wang, H.-H., Lee, W.-K., Taam, R. E., Feng, C.-C., & Lin, L.-H. 2015, ApJ,

Willett, K. W., Lintott, C. J., Bamford, S. P., et al. 2013, MNRAS, 435, 2835

Williams, T. G., Kreckel, K., Belfiore, F., et al. 2022a, MNRAS, 509, 1303 Williams, T. G., Lee, J. C., Larson, K. L., et al. 2024, ApJS, 273, 13

Williams, T. G., Schinnerer, E., Emsellem, E., et al. 2021, AJ, 161, 185

Williams, T. G., Sun, J., Barnes, A. T., et al. 2022b, ApJ, 941, L27

- Observatorio Astronómico Nacional (IGN), C/Alfonso XII, 3, E-28014 Madrid, Spain
- Sterrenkundig Observatorium, Universiteit Gent, Krijgslaan 281 S9, B-9000 Gent, Belgium
- Max-Planck-Institut für extraterrestrische Physik, Giessenbachstraße 1, D-85748 Garching, Germany
- Argelander-Institut für Astronomie, Universität Bonn, Auf dem Hügel 71, 53121 Bonn, Germany
- European Southern Observatory, Karl-Schwarzschild Straße 2, D-85748 Garching bei München, Germany
- Univ Lyon, Univ Lyon 1, ENS de Lyon, CNRS, Centre de Recherche Astrophysique de Lyon UMR5574, F-69230 Saint-Genis-Laval,
- Universität Heidelberg, Zentrum für Astronomie, Institut für Theoretische Astrophysik, Albert-Ueberle-Str 2, D-69120 Heidelberg,
- Universität Heidelberg, Interdisziplinäres Zentrum für Wissenschaftliches Rechnen, Im Neuenheimer Feld 205, D-69120 Heidelberg, Germany
- Harvard-Smithsonian Center for Astrophysics, 60 Garden Street, Cambridge, MA 02138, USA
- Elizabeth S. and Richard M. Cashin Fellow at the Radcliffe Institute for Advanced Studies at Harvard University, 10 Garden Street, Cambridge, MA 02138, USA
- National Radio Astronomy Observatory, 800 Bradbury SE, Suite 235, Albuquerque, NM 87106, USA

- Department of Astronomy, The Ohio State University, 140 West 18th Avenue, Columbus, Ohio 43210, USA
- Departamento de Física de la Tierra y Astrofísica, Universidad Complutense de Madrid, E-28040, Spain
- Max-Planck-Institut für Astronomie, Königstuhl 17, D-69117, Heidelberg, Germany
- School of Physics and Astronomy, University of St Andrews, North Haugh, St Andrews, KY16 9SS, UK
- Sub-department of Astrophysics, Department of Physics, University of Oxford, Keble Road, Oxford OX1 3RH, UK
- Université Côte d'Azur, Observatoire de la Côte d'Azur, CNRS, Laboratoire Lagrange, 06000, Nice, France
- Department of Physics and Astronomy, University of Wyoming, Laramie, WY 82071, USA
- Department of Physics, University of Connecticut, Storrs, CT, 06269, USA
- Research School of Astronomy and Astrophysics, Australian National University, Canberra, ACT 2611, Australia
- IRAP, OMP, Université de Toulouse, 9 Av. du Colonel Roche, BP 44346, F-31028 Toulouse cedex 4, France
- AURA for the European Space Agency (ESA), ESA Office, Space Telescope Science Institute, 3700 San Martin Drive, Baltimore, MD 21218, USA
- Astronomisches Rechen-Institut, Zentrum für Astronomie der Universität Heidelberg, Mönchhofstraße 12-14, D-69120 Heidelberg, Germany
- Purple Mountain Observatory, No. 10 Yuanhua Road, Qixia District, 210023 Nanjing, China
- Department of Physics, Tamkang University, No.151, Yingzhuan Rd., Tamsui Dist., New Taipei City 251301, Taiwan
- Instituto de Astrofísica de Canarias, C/ Vía Láctea s/n, E-38205, La Laguna, Spain
- Departamento de Astrofísica, Universidad de La Laguna, Av. del Astrofísico Francisco Sánchez s/n, E-38206, La Laguna, Spain
- Departamento de Astronomía, Universidad de Chile, Camino del Observatorio 1515, Las Condes, Santiago, Chile
- Faculty of Global Interdisciplinary Science and Innovation, Shizuoka University, 836 Ohya, Suruga-ku, Shizuoka 422-8529,
- Department of Astrophysical Sciences, Princeton University, 4 Ivy Ln., Princeton, NJ 08544 USA

Appendix A: Spiral galaxy sample

Table A.1. Spiral galaxy sample studied in this paper.

	$\log(M_{\star}/M_{\odot})$	$\log(SFR/[M_{\odot} \text{ yr}^{-1}])$	R ₂₅ (")	d (Mpc)	spiral morphology	bar	class
IC 1954	9.7	-0.44	89.8	12.8	M	1	С
NGC 0628	10.3	0.24	296.6	9.8	M	0	В
NGC 1300	10.6	0.07	178.3	19.0	G	1	В
NGC 1385	10.0	0.32	102.1	17.2	F	0	A
NGC 1512	10.7	0.11	253.0	18.8	G	1	C
NGC 1566	10.8	0.66	216.8	17.7	G	1	A
NGC 1672	10.7	0.88	184.6	19.4	G	1	В
NGC 2090	10.0	-0.39	134.6	11.8	G	0	C
NGC 2283	9.9	-0.28	82.8	13.7	F	1	A
NGC 2566	10.7	0.94	127.7	23.4	G	1	В
NGC 2835	10.0	0.09	192.4	12.2	G	1	C
NGC 2997	10.7	0.64	307.7	14.1	G	0	В
NGC 3507	10.4	0.00	87.5	23.5	G	1	C
NGC 3627	10.8	0.58	308.4	11.3	G	1	В
NGC 4254	10.4	0.49	151.1	13.1	M	0	В
NGC 4303	10.5	0.73	206.6	17.0	M	1	A
NGC 4321	10.7	0.55	182.9	15.2	G	1	В
NGC 4535	10.5	0.33	244.4	15.8	M	1	C
NGC 4548	10.7	-0.28	166.4	16.2	G	1	C
NGC 4731	9.5	-0.22	189.7	13.3	G	1	C
NGC 5194	10.6	0.64	411.3	8.6	G	1	В
NGC 5248	10.4	0.36	122.2	14.9	G	1	C
NGC 5643	10.3	0.41	157.4	12.7	M	1	В
NGC 6744	10.7	0.38	470.0	9.4	M	1	C

Notes. Stellar mass and star formation rates are adopted from Leroy et al. (2021b) who calculated them using the prescriptions and data from Leroy et al. (2019). These are based on GALEX and WISE radial profiles, translated to physical quantities using recipes (SFR conversion and mass-to-light ratio) designed to match the SED fitting results of Salim et al. (2016, 2018). The optical isophotal radius R_{25} is adopted from RC3 (de Vaucouleurs et al. 1991) via LEDA, and distances come from Anand et al. (2021). The spiral morphology lists the spiral family according to Buta et al. (2015) or the definitions adopted in Meidt et al. (2021) for galaxies outside the S⁴G survey ('G' stands for grand-design, 'M' for multi-armed, and 'F' for flocculent). The bar presence (1 for barred) reflects the environmental masks from Querejeta et al. (2021). The last column indicates the classification according to Fig. 5: class A implies positive mean offsets and a significant radial trend; class B corresponds to mean positive offsets but no radial trend; class C implies mean offsets compatible with zero or negative.

Appendix B: Assessing the robustness of the offset measurements

In order to study the robustness of our results, Table B.1 shows the impact of two alternative definitions of offsets. Our nominal strategy is to measure offsets in galactocentric radial bins based on the peak emission in CO and H α within each spiral arm, as illustrated by Fig. 2. This mimics the definition adopted by Egusa et al. (2009). However, for a number of reasons discussed in Sect. 5.2, these offsets are subject to very large scatter. Thus, here we consider the impact of choosing the second brightest azimuthal bin at each radius (in CO and H α , '2nd peak') instead of the actual peak, to measure how sensitive our results are to the choice of individual peaks. We also consider the weighted mean azimuth (weighted by CO and H α luminosity) for each spiral at each radius. This is expected to mitigate stochasticity associated with individual clumps at the expense of somewhat washing out the signal due to emission that is more spread out and not directly associated by the accumulation of CO due to the spiral or HII regions which are the direct product of spiral arm star formation.

The results from Table B.1 and Fig. B.1 confirm that the choice of the second brightest azimuthal bin or the weighted mean position does have a significant impact on the individual offsets. Yet, the main conclusions for a net positive offset in most galaxies and a radial trend in a few of them remains valid under these two alternatives. For the cases where we originally measured a substantial positive offset (> 100 pc), the typical change when considering the alternative definitions is of a few times 10% (median ~35–50%). As expected, the standard deviation is reduced when considering the weighted mean offset instead of the offset between peaks (from a mean of 1.5 kpc to 1.0 kpc). The galaxies that show a positive correlation between offset (θ) and radius still show a positive correlation when adopting any of the other definitions of offsets, but the Spearman rank correlation coefficient changes at the level of a few multiples of 10%. Interestingly, the derived pattern speeds are almost not affected at all by the precise definition of offsets, with a change of only a few percent.

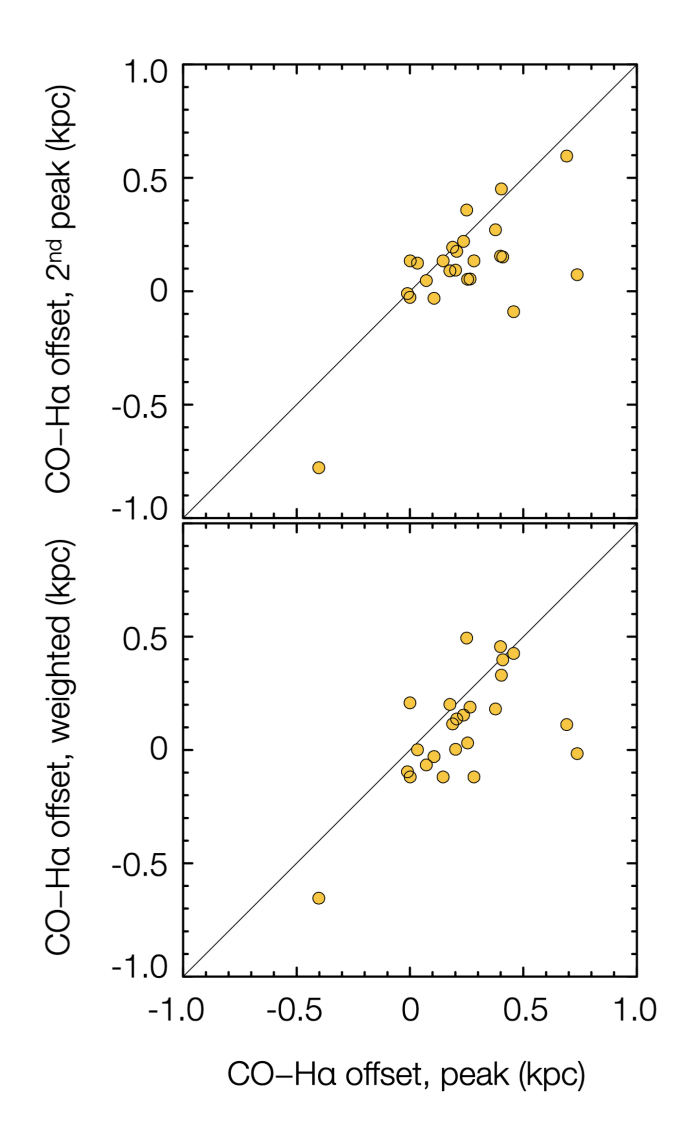
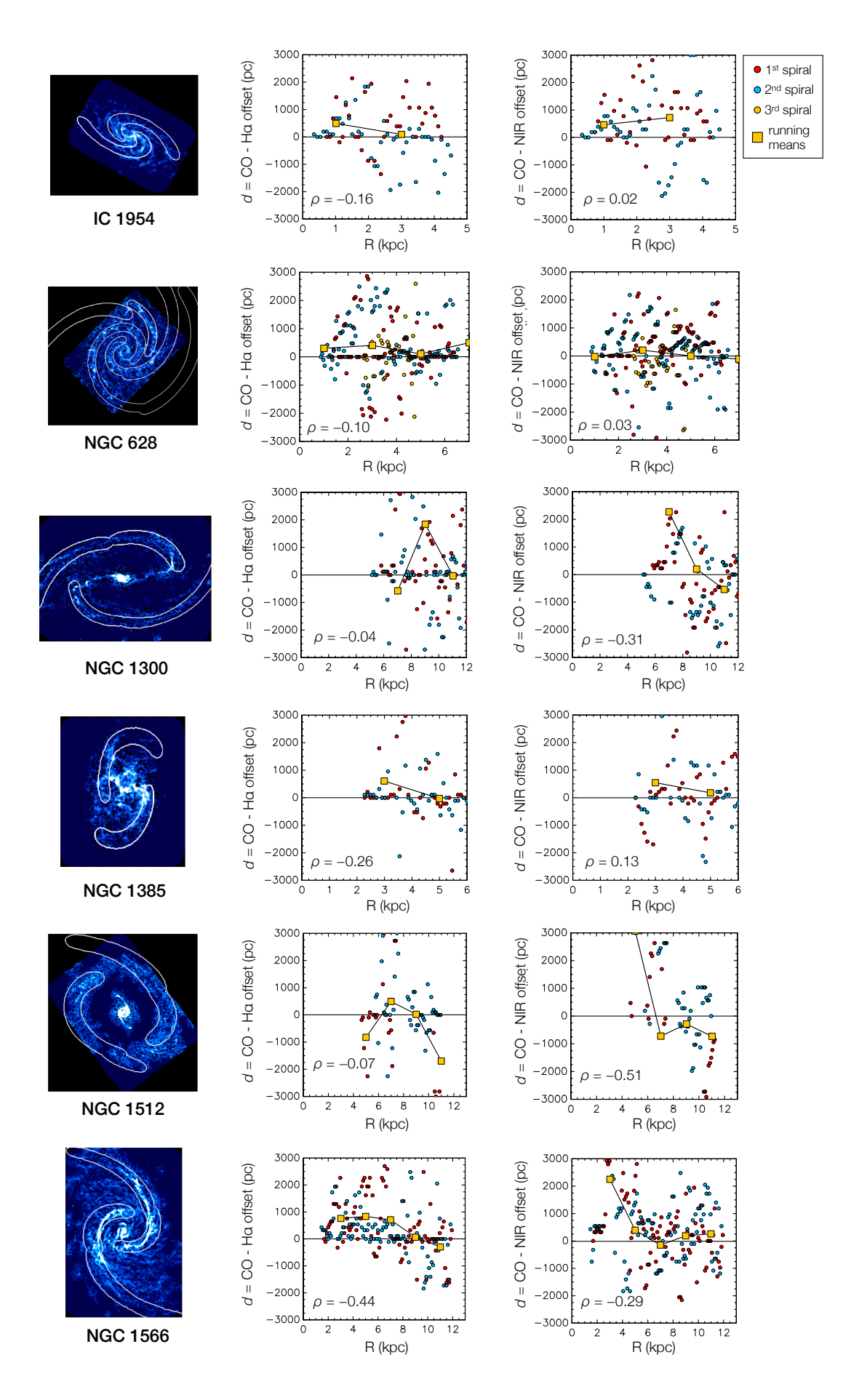


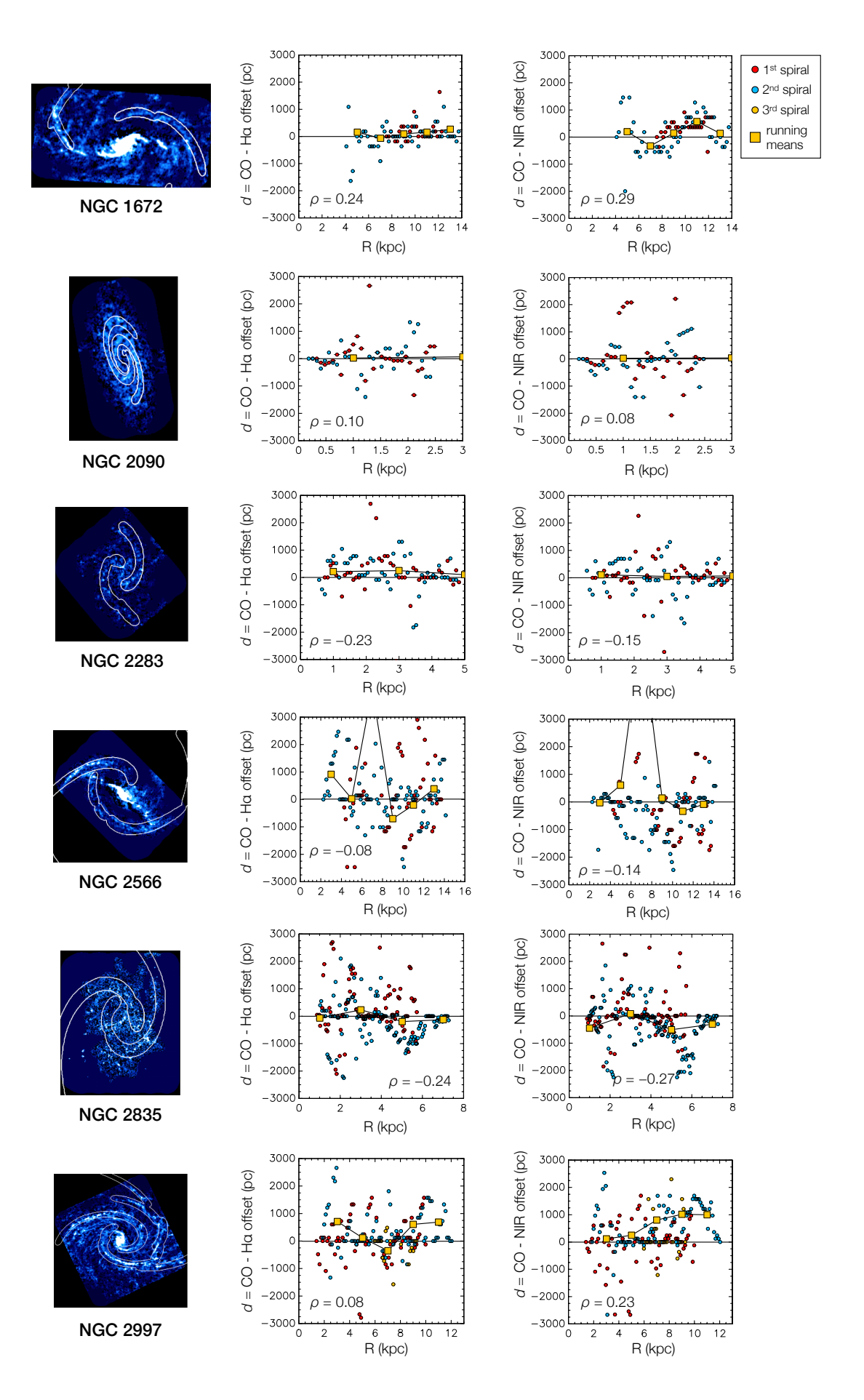
Fig. B.1. Mean CO-H α offsets based on our nominal approach (intensity peaks) compared to two alternative definitions of offsets: choosing the second brightest peak or the intensity-weighted position (see text for details). Each data point represents the mean offset per galaxy.

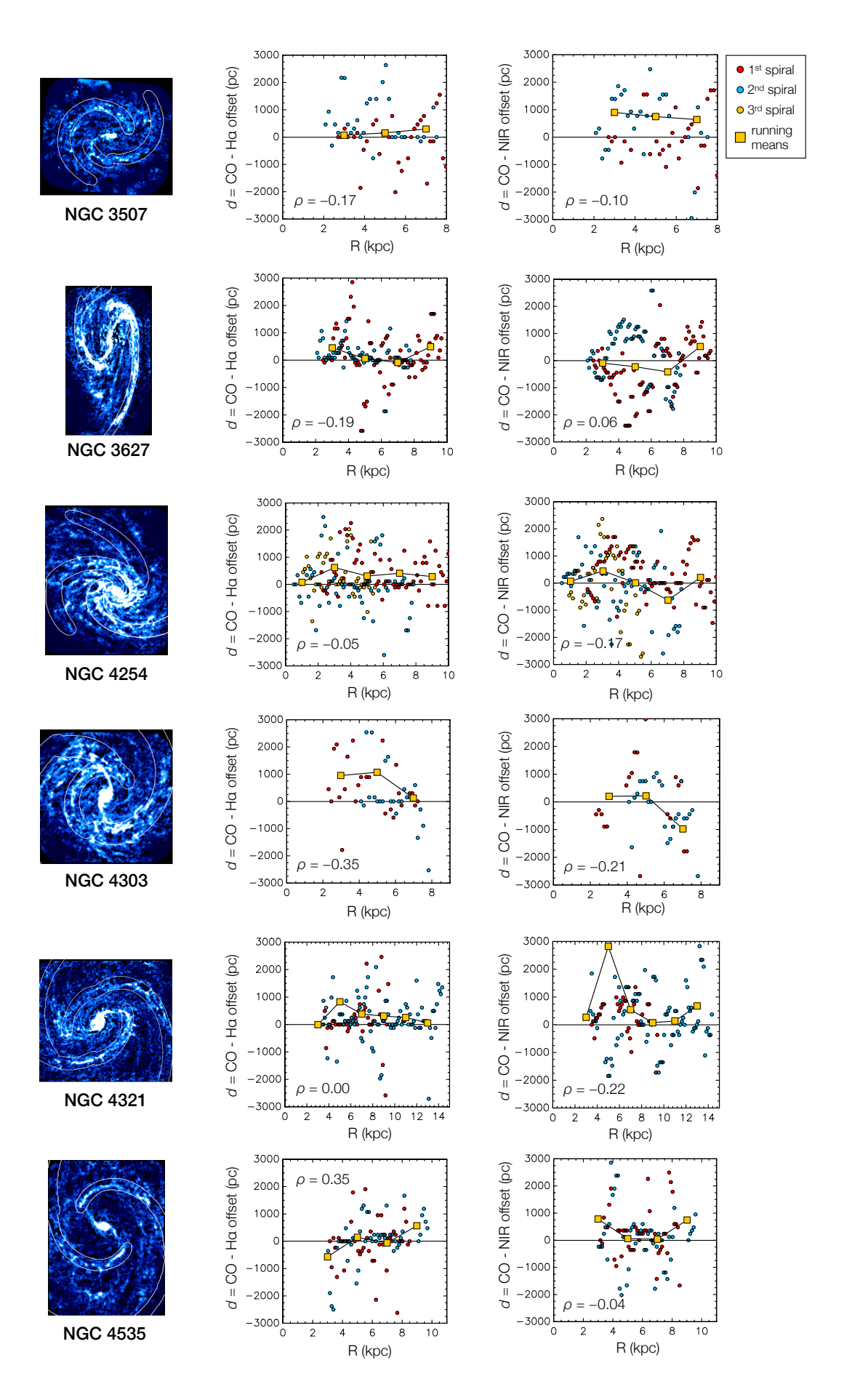
Table B.1. Impact of an alternative definition of offsets.

	$\langle heta_{ ext{CO-H}lpha} angle$		σ		ho			$\Omega_{ m P}$				
	peak	2^{nd} p.	weight	peak	2^{nd} p.	weight	peak	2^{nd} p.	weight	peak	2 nd p.	weight
IC1954	206	176	137	1040	1166	465	0.29	0.16	0.18	32.7	33.6	28.8
NGC0628	236	220	154	948	1304	333	0.15	0.02	0.20	31.7	32.7	32.4
NGC1300	457	-90	426	3587	2615	2272	-0.01	-0.11	-0.05	23.0	23.1	23.0
NGC1385	265	54	189	1040	1125	663	0.31	0.14	0.27	26.1	26.4	25.9
NGC1512	-402	-778	-654	3083	3317	3991	0.19	-0.02	0.23	21.4	21.4	21.3
NGC1566	403	451	330	1064	1119	642	0.56	0.44	0.50	25.0	24.8	24.0
NGC1672	106	-31	-29	582	565	222	-0.21	-0.19	-0.41	15.1	15.0	14.4
NGC2090	33	124	1	596	600	138	-0.14	-0.08	-0.12	147.2	-218.7	97.9
NGC2283	201	93	3	752	888	307	0.32	0.33	0.24	28.2	31.9	34.0
NGC2566	737	73	-16	5110	6712	3456	0.01	0.01	0.20	16.1	16.2	16.2
NGC2835	-11	-10	-96	852	1222	622	0.21	0.14	0.18	29.3	29.3	29.8
NGC2997	250	358	494	2135	1557	1509	-0.01	0.04	0.11	28.2	28.1	28.0
NGC3507	146	134	-119	1757	2391	717	0.23	0.12	-0.21	27.6	22.8	23.1
NGC3627	176	90	201	962	984	371	0.29	0.34	0.40	26.6	29.6	19.1
NGC4254	377	271	181	1093	1086	603	0.14	0.04	0.03	15.2	2.4	97.0
NGC4303	691	596	112	2070	2393	663	0.40	0.13	0.24	34.8	35.3	35.3
NGC4321	409	151	398	1738	1243	537	0.09	0.08	0.21	22.5	22.7	15.7
NGC4535	0	-27	208	937	1030	793	-0.29	-0.09	-0.29	27.2	27.2	27.1
NGC4548	254	53	31	896	743	269	-0.03	-0.15	-0.51	36.7	36.8	40.8
NGC4731	188	194	115	575	653	438	0.23	0.15	0.38	25.1	26.0	24.8
NGC5194	399	155	456	1111	1800	1961	-0.34	-0.07	0.04	61.5	43.8	43.4
NGC5248	72	47	-66	798	679	476	0.21	0.20	0.21	25.3	25.2	26.1
NGC5643	282	134	-119	2114	2391	717	0.00	0.12	-0.21	35.4	22.8	23.1
NGC6744	1	134	-119	1051	2391	717	0.21	0.16	0.18	23.0	22.9	23.2

Notes. Mean CO-H α offsets, their scatter, the strength of the θ - Ω correlation (Spearman rank ρ) and the implied pattern speed (Ω_P) for alternative definitions of offsets. 'Peak' represents our nominal measurement, based on the peak emission in CO and H α (see Fig. 2); '2nd peak' considers instead the azimuthal bin corresponding to the second brightest peak in CO and H α for each spiral arm at each radius; finally, 'weighted' considers the mean azimuth weighted by CO and H α luminosity for each spiral at each radius.







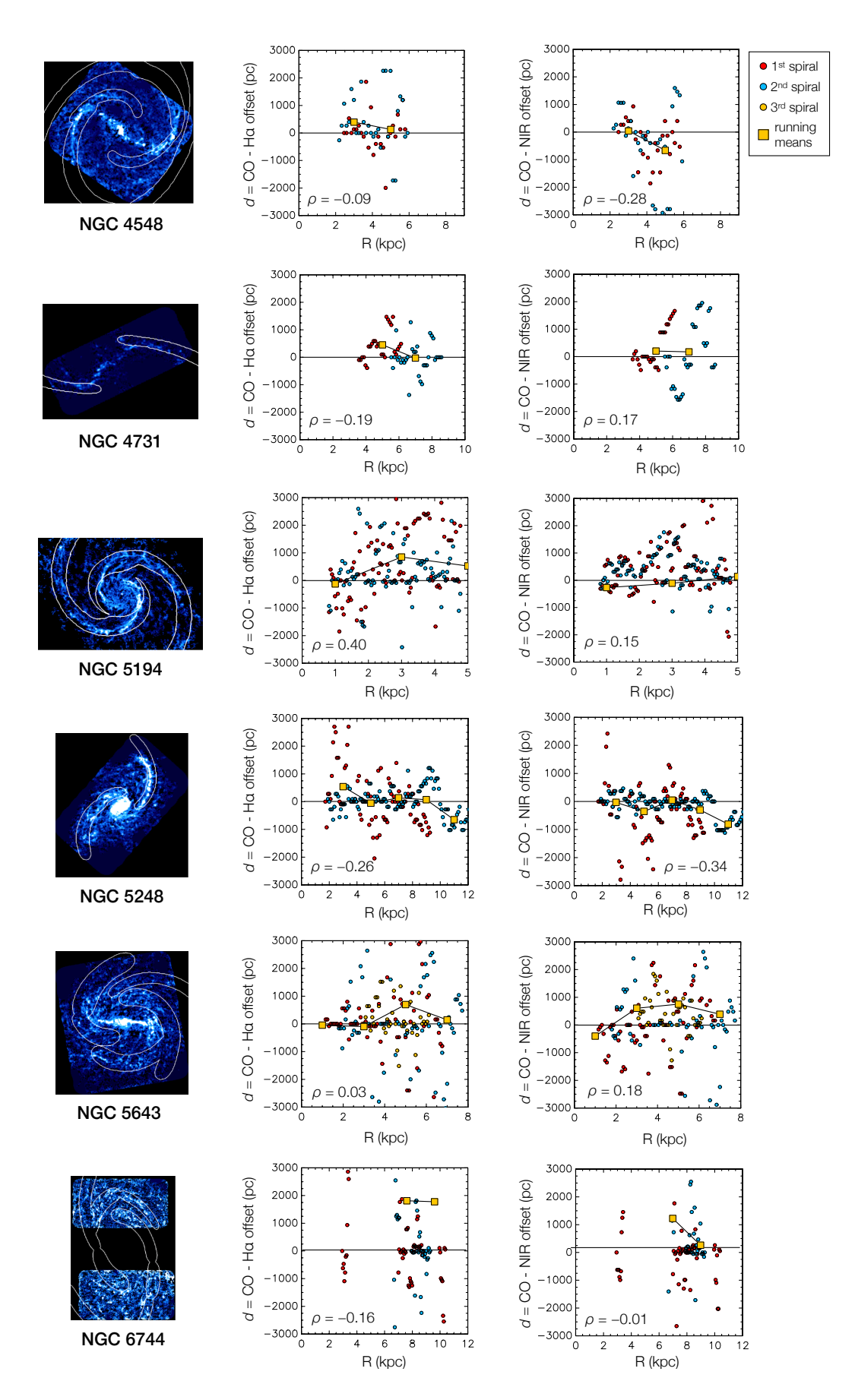


Fig. B.5. Atlas of the galaxies studied in this paper, showing the CO(2-1) map from ALMA with the spiral masks on top. In the middle panel, CO-H α offsets in parsec as a function of radius. In the right panel, equivalent CO-NIR offsets. The error bars are comparable to the size of the plotted circles. The yellow squares joined by a line show the running means in radial steps of 2 kpc.

Article number, page 21 of 21